



HAL
open science

Understanding the microstructural role of bio-sourced 3D printed structures on the tensile performance

Sofiane Guessasma, S. Belhabib, Hedi Nouri

► **To cite this version:**

Sofiane Guessasma, S. Belhabib, Hedi Nouri. Understanding the microstructural role of bio-sourced 3D printed structures on the tensile performance. *Polymer Testing*, 2019, 77, pp.105924. 10.1016/j.polymertesting.2019.105924 . hal-02331686

HAL Id: hal-02331686

<https://hal.science/hal-02331686>

Submitted on 25 Oct 2021

HAL is a multi-disciplinary open access archive for the deposit and dissemination of scientific research documents, whether they are published or not. The documents may come from teaching and research institutions in France or abroad, or from public or private research centers.

L'archive ouverte pluridisciplinaire **HAL**, est destinée au dépôt et à la diffusion de documents scientifiques de niveau recherche, publiés ou non, émanant des établissements d'enseignement et de recherche français ou étrangers, des laboratoires publics ou privés.



Distributed under a Creative Commons Attribution - NonCommercial 4.0 International License

Understanding the microstructural role of bio-sourced 3D printed structures on the tensile performance

Sofiane Guessasma¹, Sofiane Belhabib², Hedi Nouri³

¹ INRA, UR1268 Biopolymères Interactions Assemblages, F-44300 Nantes, France

² LUNAM Université Nantes Angers Le Mans, CNRS, GEPEA, UMR 6144, IUT de Nantes, avenue du Professeur Jean Rouxel, 44475 Carquefou Cédex, France

³IMT Lille-Douai, 941 rue Charles Bourseul, CS 10838, 59508 Douai, France

*Corresponding author: sofiane.guessasma@inra.fr

Abstract

This study aims at revealing the role of microstructural arrangement on the mechanical behaviour of printed PLA-Hemp using Fused Deposition Modelling (FDM). 3D printing is performed by varying the printing temperature. The laying down process is monitored using infra-red measurement. X-ray micro-tomography is used to acquire the 3D microstructure of printed PLA-Hemp. Tensile performance is determined by testing neat and notched specimens. Finite element modelling based on microstructure implementation is conducted to reveal the deformation mechanisms associated with the tensile loading. The results show a wide temperature range for printability of PLA-Hemp but **overheating effects characterises the printing using large temperatures (>220°C)**. The tensile performance is found **dependent on the printing temperature, a modified filament morphology, and an imperfect nature of the hemp-PLA interface within the filament**. Finite element results reveal particular characteristics of stress fields that superpose with underlined microstructure of filament arrangement. Despite this correlation, the low porosity level and the brittle nature of the filament do not allow strong dependence of the crack propagation on the raster orientation.

Keywords

Fused deposition modelling; PLA-Hemp composite; tensile properties; X-ray micro-tomography; finite element computation.

1. Introduction

Additive manufacturing is one of the most growing technologies dedicated to the manufacturing of complex parts by successive deposition of layers of materials [1]. Among the popular techniques used to three-dimensionally print polymer-based parts is the Fused Deposition Modelling (FDM)[2-5]. The polymeric material in the form of a wire of few millimetres in diameter is heated to the fused state and extruded through the printing nozzle to small filaments of few hundreds of microns in diameter. The relative motion of the printing nozzle with respect to the printing base and the printing temperature determine most of the characteristics of the printed polymer [6, 7]. The relative simplicity of FDM is unfortunately balanced by some drawbacks, which are basically related to the nature of material discontinuities created during the filament laying down process[8, 9]. It can be easily understood that the deposition of a filament in the three-dimensional space generates a two-dimensional discontinuity. Mechanical properties of the printed objects are closely related to the significance of this discontinuity. One important consequence is the development of a mechanical anisotropy widely reported for FDM-based parts [10-13]. For instance, the mechanical strength measured in the building direction is amongst the worst because of the lack of cohesion between successive layers. Within the plane of deposition, various deformation mechanisms are dependent on the nature of raster and its characteristics such as the raster angle [14]. Depending on the choice of the printing parameters, the loss of performance due to material discontinuities can be more or less attenuated. Early studies demonstrated the efficiency of classical approaches such as experimental designs to improve the mechanical performance of FDM-based materials [6, 15]. Recent trends are more about

compensation of the mechanical performance loss using fibre reinforcement within the filaments themselves to provide an intrinsic mechanical strength [16, 17]. Despite the huge success of FDM to process wide varieties of polymer-based composites [3, 18, 19], there is a need for in-depth studies to reveal and quantify the role of defects on the mechanical performance of printed parts. Such studies are also needed to provide a microstructural proof for a possible performance optimisation.

In this study, the printability of Polylactic acid (PLA)-Hemp composite is investigated using both experimental and numerical approaches. This material can be considered as an excellent material candidate to replace synthetic polymers in consumer goods such as single use items. Besides the environmental friendly capability, the fibre reinforcement is expected to provide mechanical strength that is usually lacking with PLA filaments. The growing interest on bio-based composites for FDM is witnessed by the recent literature work on the subject [18, 19]. Le Duigou et al. [18] considered the 3D printing of PLA/PHA matrix reinforced with wood fibres using FDM. The authors concluded that the amount of porosities generated by the FDM process and the lack of cohesiveness within the biocomposite lead together to a limited performance especially in terms of tensile strength. The studied biocomposite showed, however, capabilities of hygroscopic actuation that promote it as a potential candidate for 4D printing. Hinchcliffe et al. [20] studied the performance of printed PLA reinforced by prestressed natural jute and flax fibres. Although the study did not consider printing continuous fibres within the PLA matrix, the results demonstrated the relevance of FDM to produce structural designs with improved tensile and flexural performances.

In this study, we propose to deliver quantitative information about the 3D microstructural arrangement of the PLA-Hemp composite at different length scales. The main concern is also to provide a microstructural interpretation of the observed tensile performance and determine the efficient window for the operating temperatures to process PLA-Hemp filaments using

FDM. For this purpose, both SEM and X-ray micro-tomography imaging techniques are exploited. In addition, finite element modelling based on microstructural implementation is also considered to reveal the deformation mechanisms associated with the observed tensile response of PLA-Hemp printed structures.

2. Experimental layout

The material studied is a PLA reinforced with 10% of hemp fibres (Figure 1a). This feedstock material is provided by 3D4makers company as a wire cartridge (trade name Hemp filament) with a typical diameter of 1.75 ± 0.08 mm. The moisture content in the filament is less than 0.05%. The supplier recommended operating temperatures are between 180°C and 220°C and the suitable nozzle diameter for printing is 0.5 mm. The examination of the filament morphology indicates a rough finishing state and alignment of the hemp along the length of the filament, which suggests a forced orientation of the hemp fibres during the extrusion process.

In order to study the thermal behaviour of PLA-hemp prior printing, two scans are performed on DSC (Differential Scanning Calorimetry) equipment (DSC823e equipment - Mettler Toledo). The analysis is run within a temperature range (-40°C - 300°C) for a sample weight of 13 mg with a rate of 10 °C/min. The temperature of glass transition is determined from the second scan after releasing the thermal history.

Several types of specimens are printed using a commercial FDM solution (Replicator 2 from MakerBot). This FDM machine is equipped with a nozzle of 0.4 mm in diameter, which is smaller than the recommended one by the filament supplier. The dog-bone specimen shown in Figure 1b has a thickness of 4 mm. The filaments of two successive layers form a sequence of +45°/-45° with respect to the longitudinal dimension of the specimen. In order to improve the structural compactness of the specimens; the building resolution, (i.e., the layer height) is

adjusted to 0.2 mm meaning that the filaments are flattened by half their diameter when they exit the nozzle tip. The infill is adjusted to its maximum value (100%) to limit the study to the effect of process-generated porosity. The nozzle vertical speed is kept seven times less than the in-plane speed (150 mm/s). A raft is added to allow a better flatness and the printing of a cohesive structure (Figure 1b). The software MakerBot[®] Desktop is used to prepare the CAD files and convert them into collection of toolpaths after surface tessellation. Among the printing parameters, only the printing temperature is varied in this study according to five levels starting from 210°C and up to the maximum tolerated temperature on the equipment (255°C).

The overall density of the specimens is determined from weight measurement and volume of the real specimens. The thermal behaviour during the laying down process is approached using infrared (IR) measurements (Figure 2). For this purpose, specific specimens such as the ones shown in Figure 2b are specially designed to allow heating and cooling stages to be captured without the thermal perturbation coming from the displacement of the nozzle tip. This analysis is undertaken using an IR camera from Flir company (Flir A35 series). The resolution of the IR images is 320 x 256 pixels and the image rate is 60 Hz. The relevance of the temperature acquisition is checked by comparing the temperature reading from a contact thermocouple. The comparison outcome is a variation below 3°C of the IR reading. Image recording and processing are performed using the Flir tool software.

Up to 29 minutes are needed to print the sample shown in Figure 1b, and less than 6 minutes for the samples exhibited in Figure 2b.

The microstructural arrangement in the printed PLA-hemp is realised using X-ray micro-tomography equipment UltraTom X-ray micro-CT from Rx-Solutions. An X-ray source capable of delivering 230 KV is used. The voltage is adjusted to 80 KV for which the current intensity is 480 μ A. The 3D images (tomograms) are built using a total of 1440 radiographic

2D images using a detector that has a resolution of 1920×1536 pixels. The sample is placed at distance from the detector allowing a voxel size of $14.31 \mu\text{m}$. Less than half an hour is needed to accomplish the radiographic imaging. These are converted into a stack of 2D images (a tomogram) using a back projection reconstruction algorithm available in X-Act software from Rx-Solutions. The dimensions of the imaged structure are $1277 \times 906 \times 291$ voxels, corresponding to a physical volume of $18 \times 13 \times 4 \text{ mm}^3$. Image processing needed to isolate the features of interest is performed using the image processing software ImageJ from NIH (USA).

Mechanical characterisation is performed on both neat and notched (ratio between the notch depth and sample width is between 0.12 and 0.15) dog-bone specimens as well as on the as-received PLA-Hemp filaments. Tensile experiments are performed using uniaxial Zwick Roell machine equipped with a load cell of 10 kN (Figure 1c). The displacement rate is fixed to 5 mm/min. Optical recording of the deformation sequences is conducted during the tensile testing using a high-speed camera (Phantom V7.3 from Photonline, Marly Le Roi, 78-France). Two main imaging acquisition setups are used: full resolution (800×600 pixels) at moderate frame rate of 30 fps (frames per second) and small ROI (Region Of Interest) regions (128×80 pixels) at high speed ranging from 76,000 to 110,000 fps. The last setup is used to monitor the crack propagation in notched specimens.

Scanning Electron microscopy SEM is used to observe the main characteristics of filament arrangement near the fractured surfaces. This analysis is performed using JEOL JSM 7600F microscope under a fixed resolution of 1280×1024 pixels and with different pixel sizes ranging from $0.11 \mu\text{m}$ and $3.13 \mu\text{m}$. All samples prepared are coated with a layer of gold/palladium prior observation.

3. Modelling technique

Two finite element models are implemented based on the conversion of 3D microstructures into meshes using voxel-to-element conversion. The first model is a micromechanical model representing the tensile behaviour of the hemp-based filament (Figure 1a). The geometry of a part of the filament (diameter = 1.75 mm, length = 15 mm) is meshed using cuboid elements. The average hemp fibre volume content is adjusted to 10%. The hemp fibres are 0.53±0.09 mm and a largest lateral dimension of 90 ±10 µm according to optical observations. In addition, the hemp fibre section is considered as elliptical with a shape factor of nearly 2 (ratio between the largest and smallest semi-lengths). The material models considered are isotropic linear elastic. Young's modulus of the PLA matrix is adjusted based on the experimental value (1.0 GPa) and the modulus of the hemp bundles is varied between 5 GPa and 20 GPa, according to the known variability in hemp properties. In addition, an interfacial layer surrounding the hemp fibre is implemented to account for the partial load transfer between the PLA matrix and the hemp fibre. This layer has a varied stiffness (<1 GPa) to thickness (>16 µm) ratio. Mesh sensitivity is conducted by varying the element size from 15 µm up to 100 µm. The model size varies from 0.11×10⁶ to 47.89×10⁶ dof (degrees of freedom). Tensile boundary conditions are applied (U=0, z=0; UZ=1%×l, z=l; where l is the filament length, Z is the loading direction, UZ is the translation in Z-direction). The predicted Young's modulus is predicted for different interfacial combinations and element sizes as well as von Mises stress (σ_{Mises}) counterplots are derived.

The second finite element model is implemented to predict the tensile behaviour of the 3D printed hemp-based material. In this model, the geometry of the central part of the tensile specimens is meshed. Only the solid phase is considered for meshing. Due to the small size of the hemp fibres that cannot be captured with the acquisition resolution, a homogenised medium is used instead of a two-phase material. The voxel-to-element conversion assumes a regular meshing based on 3D structural cuboid elements defined by eight nodes and each

node is capable of displacements UX , UY and UZ in the main directions of the solid. The model size is proportional to the resolution of the tomograms. Two main computations are performed: one is related to different sampling ratios within the original tomogram and the second corresponds to the full tomogram but taken at different voxel sizes. These two types of computations are performed under linear elasticity conditions. The aim is to define the minimum volume beyond which the mechanical predictions are stable and to determine the minimum resolution at which the computations should be performed. When the two criteria about mechanical stability and resolution are met, the finite element predictions are used to study the deformation mechanisms associated with the tensile response of the printed PLA-Hemp structure. The model size is varied between 0.1×10^6 and 216×10^6 dofs (degrees of freedom) depending on the processed volume (between 43 and $16,931 \text{ mm}^3$) and the voxel size (between $14.31 \text{ }\mu\text{m}$ and $260 \text{ }\mu\text{m}$).

Tensile loading in Y-direction of the printed PLA-Hemp structure is simulated by imposing a fixed displacement UY for all nodes located at $y=L$, where L is the length of the computation domain, and fixing their lateral degrees of freedom ($UX=0$, $UZ=0$). The amount of displacement is fixed to 1% of the total length. The homologue nodes situated at $y = 0$ are all constrained against motion ($UX=UY=UZ=0$).

The reaction forces at the loaded end ($y=L$) are obtained after solving the elasticity problem using a Preconditioned Conjugate Gradient (PCG). Young's modulus is predicted for all types of computations introduced earlier. In addition, stress fields are derived. Computations are performed on a workstation equipped with 2 CPU operated at 3.0 Ghz and 1 Tbytes of RAM. The typical computation duration varies between 1 min. to 1,884 min.

4. Results and discussion

4.1. Thermal properties of hemp-based filament and laying down process

The examination of the DSC results shows that the temperature of glass transition of PLA-Hemp filament is close to 60°C, which corresponds to the glassy-rubbery transition of PLA matrix (Figure 3). Signori et al. [21] report also a glass transition of PLA close to 60°C. Within the range covering between 150°C and 180°C, the peak at about 160°C corresponds to the melting of PLA, which occurs below the operating temperatures selected for this material (between 210°C and 240°C). According to TGA scans up to 600°C reported by Ohkita et al.[22], degradation of PLA occurs only at 377°C. The thermal response of the material also shows a characteristic peak around 100°C, which is attributed to the evaporation of water from the hemp fibre. If the scan is continued to temperatures larger than 300°C, decomposition and degradation of fibre elements such as cellulose and lignin should be observed according to several reported works. Indeed, Stevulova et al.[23] shows from a larger DSC scans that three exothermic peaks centred around 312, 395, and 437°C are obtained and associated with chemical degradation of hemp hurds. Ouajai et al.[24] considered thermogravimetry analysis of untreated hemp fibres and showed a degradation of cellulose between 350°C and 400°C depending on the heating rate. Kabir et al.[25] showed through DSC measurements that untreated hemp fibre reinforced polyester presents endothermic peak between 70 and 90°C, which is related to the water evaporation. The same composite exhibits an exothermic peak between 260°C and 380°C, which is attributed to the lignin, hemicelluloses and α -cellulose degradation. The same authors concluded on a stability of the hemp fibre in the range 110°C – 200°C because of the absence of endothermic and exothermic peaks. Oza et al.[26] studied the thermal degradation using thermogravimetric analysis of PLA—hemp composite similar to the one considered in this work. The authors report a two stage kinetics corresponding to inherent moisture in hemp fibres, and fibre decomposition starting from 250°C and leading to complete degradation in the range 350°C -

360°C. The same authors report a one stage degradation for PLA starting from 300°C and ending at 400°C.

Thus, within the considered range of printing temperatures, hemp fibres can be considered as thermally stable.

The evolution of the temperature during the laying down process is shown in Figure 4 for three different printing temperatures. The filament temperature at the nozzle exit is close to 180°C and there seems to have only minor differences between the printing temperatures. The cooling down of the filament is rapid reaching temperatures as low as 40°C. The laying down process itself is smooth for all printing temperatures and there is no obvious discontinuity along the path of deposition. For a better rendering, the full sequences are provided as a supplementary material (IR_Hemp.mp4). At the end of the sequence (323 s), a larger heat accumulation can be observed for the largest printing temperature. The resulting structures shown in Figure 2 demonstrate that all attempted printing temperatures are valid for providing a cohesive structure, a flat raft and continuous deposition along the strip line that connects the end blocs. There is, however, a drawback for using printing temperatures larger than 240°C. Indeed, the low viscous state of the filaments leads to the formation of an unwanted deposition on the side of the structure which occurs when the nozzle moves to the other bloc and start a new layer. This problem can be solved by increasing the amount of retraction of the filament inside the nozzle. Thermal cycles extracted at a particular position from the strip at the mid length and mid height are shown in Figure 5 for two different printing temperatures. The alternation of peak and ground temperatures defines the thermal cycles. These are distant at the beginning of the sequence up to a characteristic time of 150s. These cycles correspond to the formation of the raft, for which the difference between the peak and ground temperatures can be as large as 130°C. The remaining cycles are the ones related to the building of the structure. During the building up stage of the structure, the difference

between the ground and the peak reaches up to 95°C, which indicates a substantial cooling down during the laying down process. There is also a marked difference between the printing temperatures that can be read from the largest magnitudes reached by the peak temperatures (Figure 5a). The plot of the average ground and peak temperatures for all printing conditions can be informative of the heat accumulation kinetics for PLA-Hemp prints. Indeed, the difference between the peak and ground temperature (ΔT) can be stated as linearly and positively correlated to the printing temperature (T_p) as follows

$$\Delta T(^{\circ}C) = -119 + 0.85 \times T_p(^{\circ}C) \quad ; \quad R^2 = 0.91 \quad (1)$$

In order to relate the positive linear trend represented by equation (1) to the heat accumulation during the laying down processing, the transient thermal behaviour of a typical FDM process is explored based according to various simulation works [27, 28]. This behaviour relies on the conservation energy criterion where the heat production by the moving energy source (the liquefier space) is balanced by the heat flux. This latter depends on the thermal conductivity and the temperature gradient. Thus, the thermal dissipation by both conduction and convection is responsible for the ground temperature at the completion of each thermal cycle (Figure 5b). The peak temperature is measured when the source is the closest to the position where the temperature is sensed and more related to the source term. As there is a larger thermal energy available for a high printing temperature, the positive trend in equation (1) means that, for a given thermal cycle, a larger accumulation of the thermal energy is obtained. Figure 5b shows that the heat accumulation trend is positive starting from 210°C up to 255°C. This trend is to be related to the success of PLA-Hemp printing as shown in Figure 2b.

4.2. Intrinsic tensile performance of hemp fibre-PLA composite

Tensile performance of the PLA-Hemp filaments is illustrated in Figure 6. From Figure 6a, the deformation sequence shows a brittle fracture and only a limited loading is sufficient to

achieve the rupture of the filament. There is, in addition, no obvious signs of reduction in section, which can be expected from other types of filaments such as PLA. In Figure 6b the tensile behaviour of both PLA and PLA-hemp are reported for a collection of wires. For the PLA-hemp filament, tensile strength above 50 MPa is obtained but large differences between replicates are also observed. The tensile strength of PLA-hemp is found comparable to typical values for acrylonitrile butadiene styrene (ABS) (30 – 50 MPa) and PLA (48 – 60 MPa) [11, 12]. The experimental results for PLA in Figure 6b show that the PLA tensile strength is as large as 54 ± 0.2 MPa. This is slightly larger than the one achieved for PLA-hemp (50 ± 3 MPa). Young's modulus of PLA-hemp (Table 1) is also smaller than the value achieved for PLA (1092 ± 136 MPa). The most significant difference between the two filaments is related to the elongation at break. For PLA, the measured property reaches 55 ± 18 %, which is much larger than the one of PLA-hemp (Table 1). Another difference is related to the dispersion of the results. All measured properties for PLA-hemp such as Young's modulus, tensile strength, and elongation at break all exhibit a large dispersion. The data collected in Table 1 show that this dispersion reaches 18%. This dispersion is related to the variability in the hemp fibre properties that is widely reported [29, 30]. The overall tensile behaviour of the PLA-Hemp filament can be considered as elastic with minor plasticity and a quasi-brittle fracture. In addition, multiple fracture events can be observed within the elastic stage, which can be attributed to fibre fracturing and fibre-matrix decohesion. Thus, despite the addition of hemp fibres that are supposed to improve the filament behaviour of the composite, Figure 6b suggests that there is an evident lack in both stiffness and strength of PLA-hemp filament compared to PLA that can be only explained by weak interface properties between the PLA matrix and the hemp reinforcement.

The low intrinsic performance of PLA-Hemp filament is mainly related to the quality of the natural fibres. Indeed, the large amount of defect reported for untreated natural fibre affects

negatively both the stiffness and tensile strength [30]. In addition, the fibre length and the interfacial properties are also key factors that lower the performance. The finite element results of the micromechanical model representing the tensile behaviour of the hemp-based filament further demonstrate the significance of the interface properties. Figure 7a shows that morphology of the hemp fibre can be reasonably approached when the element size is smaller than $37\ \mu\text{m}$. For these models, the elliptical shape of the hemp fibre is better described and the interfacial layer as well. Figure 7b shows that the predicted Young's modulus of the hemp-based filament becomes mesh independent for element sizes as small as $37\ \mu\text{m}$. If only perfect interface properties are implemented and considering a hemp bundle modulus close to 20 GPa (according to the result by Mwaikamb et al. [31]), the predicted Young's modulus of the filament is 2.54 GPa. Considering that the hemp bundle quality may lead to a lower hemp fibre modulus of 5 GPa, the predicted filament modulus is 1.46 GPa. In both situations, the predicted modulus based on perfect interface is lower than the experimental modulus reported in Table 1. Figure 7c shows the predicted filament modulus based on imperfect interface properties using different combinations of interface stiffness / thickness ratios and three different hypothesis of hemp modulus. Figure 7c shows that a low filament modulus can be achieved by decreasing the interface stiffness / thickness ratios irrespective of the variability in the hemp bundle properties. The experimental Young's modulus is matched when the interface stiffness / thickness ratio is as small as $0.3\ \text{MPa}/\mu\text{m}$ for a hemp Young's modulus of 5 GPa. This ratio is much lower for a better hemp quality.

4.3. Structure and tensile properties of printed hemp-PLA

In terms of apparent density, limited variations close to $1.1\ \text{g}/\text{cm}^3$ are obtained (Table 1). The density of the filament itself is rather small compared to technical data for PLA ($1.24\ \text{g}/\text{cm}^3$). The minor change in density also indicates a small porosity content that varies between 3%

and 9 % depending on the printing temperature. The samples printed at a low temperature (<230°C) trigger, in average, a slightly denser structures compared to the one printed at higher temperatures (>220°C). These also correspond to the recommended temperatures by the supplier.

Figure 8 shows typical optical micrographs, which detail the modification of the PLA-hemp composite morphology induced by processing. The hemp fibres within the filament are still aligned along the filament length and thus their relative orientation with respect to the printed part follows the raster orientation. This observation holds for both low (<230°C) and high (>220°C) printing temperatures. Through the part thickness, the fibres are normal to building direction. The main difference between the low (Figure 8a) and high (Figure 8b) printing temperatures is the over-heating signs that are characterised by a local modification of the filament section and the presence of a pasty morphology across the thickness for temperatures larger than 220°C.

Typical deformation sequences for neat and notched specimens under tensile loading are shown in Figure 9. The corresponding sequences are provided as supplementary materials (Neat_PlaHm.mp4 and Notched_PlaHm.mp4). The examination of the deformation of neat PLA-Hemp printed sample (Figure 9a) shows no evident sign of damage that follows the raster orientation (-45° on the surface in front of the camera). In addition, the rupture is quasi-brittle and instable cracking advances in a predominant mode I propagation. High speed camera recording of notched specimens during the tensile loading confirms slight jagged crack propagation and a predominant opening mode. Even with notches as small as 1.2 mm, the crack does not deviate from the transverse direction. Its observed displacement rate exceeds 927 m/s.

Figure 10 depicts the mechanical response for all studied conditions including neat and notched PLA-Hemp specimens. The printing conditions cover a printing temperature range

between 210°C and 240°C. All curves demonstrate an elastic behaviour with limited plastic strain and abrupt rupture. A regular increase of the tensile performance is observed when the printing temperature is increased (Figure 10a). Despite this improvement, the data extracted from the tensile response indicate that, for all conditions, there is evidence of mechanical performance loss. This loss in mechanical performance is, however, significantly reduced by the increase of the printing temperature, despite the results related to the apparent density. Young's modulus, tensile strength and elongation at break are reduced by 21%, 22% and 21% when the printing temperature is set to the lowest value. The same loss in performance reduces to only 7%, 4% and 12% for the highest printing temperature. The examination of the results given in Table 1 shows that some apparent correlations between the porosity content and the mechanical parameters are likely to be misleading. Indeed, these suggest that the performance improves with the increase of the porosity content. In fact, this improvement calls for other reasons, which are related to the improvement of the bonds between the filaments. The increase of the porosity content is only to be related to over-heating issues that modify the form of the filament during the laying down process. This hypothesis is subjected to further discussion using a mathematical model of the filament arrangement based on 3D imaging observations.

The mechanical response of notched specimens shows the same overall trend of performance improvement with the increase of printing temperature (Figure 10b). The fracture toughness derived from the curves in Figure 10b varies between $2.15 \text{ MPa}\times\text{m}^{1/2}$ and $2.8 \text{ MPa}\times\text{m}^{1/2}$.

There are no available data on the fracture strength of the raw material to provide estimation about the loss in performance with respect to crack resistance properties.

Figure 11 compares the performance of the studied printed material with data of other polymers collected from the literature about [3, 4, 10, 12, 13, 15, 32-42]. Young's modulus of printed PLA-Hemp is found larger than typical values for copolyester, nylon. But it is also

found lower than ABS, polycarbonate (PC) and even PLA (Figure 11a). The tensile strength of printed PLA-Hemp has a better ranking compared to the other polymers especially polypropylene (PP), ABS, copolyester, Polyethylene terephthalate glycol-modified (PETG) and even nylon (Figure 11b). Few data are available for crack toughness (Figure 11c). The general tendency highlights a better performance for PLA-Hemp compared to ABS, copolyester and ABS.

Examination of the fractured surfaces using SEM shows characteristics of micro- and macro-arrangement of the printed material that are discussed hereafter using different magnifications (Figure 12). Under a low magnification (x30), the characteristics of the filament arrangement can be clearly distinguished. The filament themselves appear tough with a substantial amount of surface porosities. The fractured surface does not demonstrate signs of significant filament tearing or stretching. These remain as a cohesive structure. The fractured area is rough, shows signs of brittle fracture with a topography that has no evident correlation with the raster or filament arrangement at the ruptured zone. It is, however, decorated with a microscopic void structure with typical sizes between 30 μm and 100 μm . These voids may originate from the tearing of the fibres, which have the same characteristic dimension. A close look at the void network at a higher magnification (x35) shows that hemp fibre tearing occurs at different locations such as the one framed and further magnified in the same micrograph. In the two last SEM micrographs taken at higher magnifications (x150, x400), the mesostructure of the hemp fibre is observed. The rough aspect of the fibres and the presence of several surface flaws suggest that hemp fibres are untreated, which is in line with the observed low performance of the filament (Figure 6). These micrographs well show the interfacial decohesion between PLA matrix and hemp fibres as a main deformation mechanism contributing to the failure of the printed material. It can be concluded at this stage that the observed porosity within the filament can be related to the change in the filament morphology

by processing, which is driven by hemp fibre/matrix decohesion. This porosity cannot be only explained by a genuine porosity of the feedstock material.

4.4. Microstructural arrangement of 3D printed hemp-PLA

Figure 13 shows the result of 3D imaging using X-ray micro-tomography for a printed PLA-Hemp at 230°C. Figure 13a depicts the three typical cross-section views of the tomogram, namely the plane of construction X-Y, and the two other orthogonal planes Y-Z and X-Z that contain both the building direction Z. The dark grey levels correspond to porosity features and external void. The light ones are associated with the hemp fibres.

The plane of construction shows a remarkable feature, which is the presence of three populations of process-induced porosity. The first one is induced by the gap between the filaments and extends over the millimetre scale. The second one is generated inside the filament by the space left by the hemp fibres. This space can be genuine to the fabrication of the filament themselves or induced by the extrusion and stretching of the wire during the printing process. This type of defect has a typical dimension below 100 µm. The last type of defect is related to the abrupt change in trajectory when the nozzle reaches the position of the external frame. A characteristic porosity forms at the connection between the raster and the frame, which is relatively larger than the internal porosity (between 0.8 mm and 1.2 mm).

The examination of the orthogonal planes YZ and XZ shows also that the internal porosity has a significant connectivity in the building direction. This is a clear evidence of the low performance expected for a loading performed in the building direction.

Because the external air and the porosity share the same grey levels, a threshold at these levels followed by flooding performed from the outer areas allows the isolation of the internal porosity. Figure 13b shows the result of such processing, which highlights the layered structure of PLA-Hemp printed specimen and the presence of a regular network of internal

porosity. The porosity content is 4.3%, which is slightly smaller than the amount achieved from the density measurement (5.0%).

The correlation between the printing temperature and the porosity content can be derived from the density data in Table 1. Using the same fitting procedure introduced earlier for the mechanical parameters, the following expression is obtained

$$f(\%) = -30 + 0.16 \times T_p(^{\circ}C) ; \quad R^2 = 0.75 \quad (2)$$

Despite the relative scatter of the results, the porosity content can be stated as linearly correlated to the printing temperature. The positive correlation seems to oppose the idea of improving the density of the printing material when the printing temperature increases. This is in fact true as long as the printing temperature is below 210°C as recommended by the supplier and largely admitted for PLA filaments. For higher temperature ranges, the additional overheating of the filament contributes to change in the filament morphology during the laying down process and some waviness occurs as shown in Figure 14a that induces locally a modification of the filament section. This change in the filament morphology is not compensated by a varied layer height for the prescribed printing temperature. The positive correlation between the printing temperature and the mechanical performance is rather related to an effect of the printing temperature on the quality of the bound.

The connectivity of the porous network reaches only 3%, which means that the largest pore structure represents only few percent of the entire network. In order to have an idea about the spatial heterogeneity of the porosity, the porosity content along the length, width and depth of the PLA-Hemp structure are exploited. Figure 15 shows these profiles where the lengths in the abscise axis are expressed as a percent from the full dimensions. The profile along the thickness forms a U-shape where peak porosities larger than 6% are observed at the end points. These peak values correspond to the surface porosity. Along the width of the specimen, the porosity content goes from a ground value at the frame to a first peak value of

about 4% that is associated to the porosity between the raster and the frame and finally the largest magnitude at the centre position (largest peaks of about 6%). The porosity content profile along the length of the specimen shows alternation of peak and valley values that are characteristics of the raster. The peak values correspond to the largest alignment of the porosity in the orthogonal plane YZ and the valley values represent the largest filament connectivity.

In order to explore furthermore the relationship between the porosity distribution and the printing temperature, a model of porosity arrangement is proposed in Figure 14a. This model considers the main features extracted from X-ray micro-tomography imaging. The first feature is the shape modification of the filament during the laying down process induced by the filament stretching under over-heating conditions. This modification is, firstly, triggered by a layer height much lower the filament diameter. This is accounted for using the ellipse form approximation of the filament section (semi-lengths a and b). The filament shape modification is, secondly, controlled by the filament waviness represented by the parameter w . The second feature of the model is the porosity within the filament, which represents up to fifth of the total amount of porosity. In the proposed mathematical model of the microstructural arrangement (Figure 14b), the porosity within the filament is modelled as spherical voids with varied size between $50\ \mu\text{m}$ and $200\ \mu\text{m}$ and an average diameter of $100\ \mu\text{m}$. The parts in blue refer to the necking that develops between adjacent filaments during the laying down process. Figure 14c shows the achieved correlation between the generated porosity network and the printing temperature based on the mathematical model and X-ray micro-tomography data. The distribution is obtained by applying a numerical granulometry technique to the generated microstructure (Figure 14b). The model parameters (a/b between 0.5 and 0.68; $\Delta a/a$ and $\Delta b/b$ between 0.2 and 0.27; $w = 94\ \mu\text{m}$, image size = 4.8 mm) are adjusted to fit the experimental porosity content given in Table 1 for each printing

temperature. The porosity size distribution in the cumulative form shows that the largest pore size captured by the granulometry technique is below 250 μm . The results show that the larger frequencies are obtained for the highest temperature. This is explained by a larger perturbation in the filament arrangement due to the over-heating. This explanation does not hold, however, for the intermediate temperature 230°C. Despite this discrepancy, the model suggests that the use of low printing temperatures generates a low perturbation in the filament arrangement, which in turn allows a low porosity content.

4.5. Predicted behaviour of 3D printed hemp-PLA

Finite element computation based on the implementation of the 3D microstructure is discussed hereafter. The predictions detailed in the following are related to the exclusive effect of the process-induced porosity on the tensile performance of PLA-Hemp printed structures. Because of the relative low resolution to handle the structure of fibres, these are embedded in the properties of the solid phase as earlier explained.

Figure 16 depicts the influence of the sampling on the spatial distribution of the normal stress component σ_{YY} , where Y represents the direction of tensile loading. The predictions are related to cubic volumes that are cropped from the centre of the acquired 3D image of the PLA-Hemp specimen with a fixed element size of 14.31 μm . The size of the models treated in Figure 16 varies between 0.39×10^6 dof and 43.5×10^6 dof. The main characteristic of the stress field is the alternation of positive and negative stresses close to the porous structure. Despite the implementation of tensile loading conditions, the presence of negative stresses indicates a tendency for filament alignment in the loading direction. Because of the misorientation of these filaments in the raster with respect to the loading direction ($-45^\circ/+45^\circ$), the realignment causes compressive stresses at the joints between the filaments.

Another characteristic feature of the stress field is its spatial regularity that tends to be consistent with cropped sizes larger than 1 mm.

Figure 17 shows the predicted stress distributions for the same normal stress component σ_{YY} of the entire PLA-Hemp printed structure at different resolutions (voxel size varied between 14.31 μm and 260 μm). The size of the models increases from 0.1×10^6 dof to 216.3×10^6 dof, accordingly. With the smallest voxel sizes, the porosity content is expected to decrease more significantly because the averaging process during downsizing favours the predominant phase. For instance, at a voxel size of 260 μm , the porosity content is 3.4 % for a sample printed at 230°C. This is 1.60% lower than the expected content (Table 1). The change in porosity content has a consequence on the stress distribution within the printed samples. For a voxel size of 143 μm , the stress heterogeneity that takes place within the thickness of the specimen is not well captured. In addition, the stress distribution within the plane of construction is not smooth enough to differentiate between the stress levels in the raster and the frame. From a voxel size of 57 μm , the microstructural effect on the stress heterogeneity becomes more visible. For instance, there is an alternation of low and high stress levels near the porosities generated at the frame. This stress heterogeneity develops along the full length of the specimen. In addition, stress localisation within the raster takes place between the filaments triggered by the stress concentrators represented by the voids between the filaments. The regions of high stress extend over the width of the specimen and follow exactly the raster orientation. It is believed that the jagged rupture observed experimentally is obtained because of the connectivity between these regions of higher stresses. The reason for not allowing a further crack extension in the direction of filament is because of the low porosity level that tends to limit the shearing effect at the junction and promote more a predominant opening mode.

Figure 18 depicts the error committed for the evaluation of Young's modulus for an increasing resolution and specimen volume. The error is measured with respect to the prediction of Young's modulus for the original resolution (voxel size of 14.31 μm) and the full size specimen (typical volume: $14.2 \times 11.8 \times 3.5 \text{ mm}^3$). Figure 18a demonstrates that a large error is expected when the voxel size is large than 100 μm . This scatter is attributed to a poor microstructural representation that affects the stiffness prediction, for instance, the underestimation of the effect porosity level especially the one within the filaments.

Figure 18b shows that the effect of the specimen volume is rather small compared to the effect of resolution. A large stability of Young's modulus is attested by the relative low error of less than 2% even for volumes as small as $340 \mu\text{m}^3$. This large stability is due principally to the combined effect of a low porosity level and a regularity of the filament arrangement.

4. Conclusions

Printability of PLA-Hemp is proved to be possible in FDM over a large range of printing temperatures, typically between 210°C and 240°C thanks to the heat accumulation trend depicted from infra-red measurements. The relative thermal stability of hemp fibres, the presence of water and the low intrinsic performance of the filaments are the main physical characteristics associated with the lying down process of PLA-Hemp material. Although the hemp fibre orientation prior printing remains aligned along the length of the filament, reinforcement of the filament by the presence of hemp fibres is not effective as suggested from the comparison between PLA and PLA-hemp filament properties. The micromechanical model of the hemp-PLA suggests a weak interfacial properties that contribute to the change of the filament morphology and properties after printing. The development of a porosity within filament with a typical size smaller than 100 μm , can be related to the combination of inhomogeneous tearing and interfacial decohesion between the PLA matrix and the hemp fibres. The change of the filament morphology is also triggered by the highest printing

temperatures as a pasty-like laying takes place together with a varied filament section. X-ray micro-tomography shows that the amount of porosity generated by the printing process is low (from 3% to 9%, depending on the printing temperature). According to the mathematical model of the filament arrangement issued from 2D and 3D observations, the large porosity network associated with large printing temperatures with typical void sizes within the raster lower than 1mm and between the raster and the external frame (between 0.8 mm and 1.2 mm) can be interpreted as a consequence of an over-heating that locally modifies the filament morphology and the laying characteristics. From the mechanical viewpoint, the large printing temperatures improve the cohesion between the adjacent filaments in a way that only a minor loss in the mechanical performance is observed. For lower printing temperatures, this loss in tensile performance is of the order of 20% is expected with low printing temperatures cannot be explained by a low connectivity generated between the porosities (about 3%) but rather than a lack of cohesion between filaments as suggested by the finite element analysis. This study concludes also on a hierarchical influence of different levels of microstructural arrangements. The large stretching capabilities of PLA are altered by the presence of hemp fibres or more exactly the weak PLA/hemp interface properties. When combined to the filament arrangement characteristics within the plane of construction, the induced stress localisation from tensile loading reads as an alternation of negative and positive stresses. This type of stress localisation proved by finite element computation is induced by the tendency of the filaments to realign with the loading direction. The limited stretching of the hemp-based filament combined with the stress localisation triggers a brittle failure and predominant opening mode.

Declaration of interest

The authors declare no conflict of interest.

Author contributions

Dr. Sofiane Guessasma contributed to the overall management of the FDM processing and experimental testing designs. He also contributed to the mechanical testing experiments, to the X-ray micro-tomography analysis, interpretation of experimental data, and contributed substantially to the drafting the article. Dr. Sofiane Belhabib contributed to the mechanical testing experiments, to the analysis, and interpretation of experimental data. He also partly drafted the manuscript. Dr. Hedi Nouri contributed to the X-ray micro-tomography imaging, and draft checking.

Funding source

This work is conducted in the framework of SFR IBSM federation N° 4202.

Acknowledgment

The authors are thankful to Miss. Khaoula Abouzaid from INRA for technical assistance in partly preparing and conducting the experimental tests. The authors express their gratitude to Dr. Gael Colomines from the University of Nantes for conducting the DSC measurements. The authors would like to thank Dr. David Bassir from UTBM for technical assistance with the materials selection, and Dr. Boubakeur Mechri for valuable discussion about infra-red measurements.

5. References

- [1] T.D. Ngo, A. Kashani, G. Imbalzano, K.T.Q. Nguyen, D. Hui, Additive manufacturing (3D printing): A review of materials, methods, applications and challenges, *Composites Part B: Engineering*, 143 (2018) 172-196.
- [2] M.C. Wurm, T. Möst, B. Bergauer, D. Rietzel, F.W. Neukam, S.C. Cifuentes, C. von Wilmowsky, In-vitro evaluation of Polylactic acid (PLA) manufactured by fused deposition modeling, *Journal of biological engineering*, 11 (2017) 29.
- [3] F. Ning, W. Cong, J. Qiu, J. Wei, S. Wang, Additive manufacturing of carbon fiber reinforced thermoplastic composites using fused deposition modeling, *Composites Part B: Engineering*, 80 (2015) 369-378.

- [4] O. Carneiro, A. Silva, R. Gomes, Fused deposition modeling with polypropylene, *Materials & Design*, 83 (2015) 768-776.
- [5] K. Szykiedans, W. Credo, D. Osiński, Selected Mechanical Properties of PETG 3-D Prints, *Procedia Engineering*, 177 (2017) 455-461.
- [6] A. Alafaghani, A. Qattawi, B. Alrawi, A. Guzman, Experimental Optimization of Fused Deposition Modelling Processing Parameters: A Design-for-Manufacturing Approach, *Procedia Manufacturing*, 10 (2017) 791-803.
- [7] O. Lužanin, D. Movrin, M. Plančak, Experimental investigation of extrusion speed and temperature effects on arithmetic mean surface roughness in fdm-built specimens, *Journal for Technology of Plasticity*, 38 (2013).
- [8] H. Nouri, S. Guessasma, S. Belhabib, Structural imperfections in additive manufacturing perceived from the X-ray micro-tomography perspective, *Journal of Materials Processing Technology*, (2016).
- [9] S. Guessasma, W. Zhang, J. Zhu, S. Belhabib, H. Nouri, Challenges of additive manufacturing technologies from an optimisation perspective, *International Journal for Simulation and Multidisciplinary Design Optimization*, 6 (2016) A9.
- [10] N. Aliheidari, R. Tripuraneni, A. Ameli, S. Nadimpalli, Fracture resistance measurement of fused deposition modeling 3D printed polymers, *Polymer Testing*, 60 (2017) 94-101.
- [11] B. Anna, G. Selçuk, Mechanical characterization of parts fabricated using fused deposition modeling, *Rapid Prototyping Journal*, 9 (2003) 252-264.
- [12] C. Casavola, A. Cazzato, V. Moramarco, C. Pappalettere, Orthotropic mechanical properties of fused deposition modelling parts described by classical laminate theory, *Materials & Design*, 90 (2016) 453-458.
- [13] S.-H. Ahn, M. Montero, D. Odell, S. Roundy, P.K. Wright, Anisotropic material properties of fused deposition modeling ABS, *Rapid prototyping journal*, 8 (2002) 248-257.

- [14] S. Guessasma, S. Belhabib, H. Nouri, O. Ben Hassana, Anisotropic damage inferred to 3D printed polymers using fused deposition modelling and subject to severe compression, *European Polymer Journal*, 85 (2016) 324-340.
- [15] J. Torres, J. Torres, M. Cole, M. Cole, A. Owji, A. Owji, Z. DeMastry, Z. DeMastry, A.P. Gordon, A.P. Gordon, An approach for mechanical property optimization of fused deposition modeling with polylactic acid via design of experiments, *Rapid Prototyping Journal*, 22 (2016) 387-404.
- [16] P. Parandoush, D. Lin, A review on additive manufacturing of polymer-fiber composites, *Composite Structures*, 182 (2017) 36-53.
- [17] X. Wang, M. Jiang, Z. Zhou, J. Gou, D. Hui, 3D printing of polymer matrix composites: A review and prospective, *Composites Part B: Engineering*, 110 (2017) 442-458.
- [18] A. Le Duigou, M. Castro, R. Bevan, N. Martin, 3D printing of wood fibre biocomposites: From mechanical to actuation functionality, *Materials & Design*, 96 (2016) 106-114.
- [19] M. Milosevic, D. Stoof, K. Pickering, Characterizing the Mechanical Properties of Fused Deposition Modelling Natural Fiber Recycled Polypropylene Composites, *Journal of Composites Science*, 1 (2017) 7.
- [20] S.A. Hinchcliffe, K.M. Hess, W.V. Srubar, Experimental and theoretical investigation of prestressed natural fiber-reinforced polylactic acid (PLA) composite materials, *Composites Part B: Engineering*, 95 (2016) 346-354.
- [21] F. Signori, M.-B. Coltelli, S. Bronco, Thermal degradation of poly(lactic acid) (PLA) and poly(butylene adipate-co-terephthalate) (PBAT) and their blends upon melt processing, *Polymer Degradation and Stability*, 94 (2009) 74-82.
- [22] T. Ohkita, S.-H. Lee, Thermal degradation and biodegradability of poly (lactic acid)/corn starch biocomposites, *Journal of Applied Polymer Science*, 100 (2006) 3009-3017.

- [23] N. Stevulova, A. Estokova, J. Cigasova, I. Schwarzova, F. Kacik, A. Geffert, Thermal degradation of natural and treated hemp hurds under air and nitrogen atmosphere, *Journal of Thermal Analysis and Calorimetry*, 128 (2016) 1649-1660.
- [24] S. Ouajai, R.A. Shanks, Composition, structure and thermal degradation of hemp cellulose after chemical treatments, *Polymer Degradation and Stability*, 89 (2005) 327-335.
- [25] M. Kabir, H. Wang, F. Cardona, T. Aravinthan, Effect of chemical treatment on the mechanical and thermal properties of hemp fibre reinforced thermoset sandwich composites, (2010) 439-444.
- [26] S. Oza, H. Ning, I. Ferguson, N. Lu, Effect of surface treatment on thermal stability of the hemp-PLA composites: Correlation of activation energy with thermal degradation, *Composites Part B: Engineering*, 67 (2014) 227-232.
- [27] Y. Zhang, V. Shapiro, Linear-Time Thermal Simulation of As-Manufactured Fused Deposition Modeling Components, *Journal of Manufacturing Science and Engineering*, 140 (2018) 071002.
- [28] H. Xia, J. Lu, S. Dabiri, G. Tryggvason, Fully resolved numerical simulations of fused deposition modeling. Part I: fluid flow, *Rapid Prototyping Journal*, 24 (2018) 463-476.
- [29] J. Beaugrand, S. Guessasma, Scenarios of crack propagation in bast fibers: Combining experimental and finite element approaches, *Composite Structures*, 133 (2015) 667-678.
- [30] J. Beaugrand, S. Guessasma, J.-E. Maigret, Damage mechanisms in defected natural fibers, *Scientific Reports*, 7 (2017).
- [31] L.Y. Mwaikambo, M.P. Ansell, Mechanical properties of alkali treated plant fibres and their potential as reinforcement materials. I. hemp fibres, *Journal of Materials Science*, 41 (2006) 2483-2496.

- [32] N.G. Tanikella, B. Wittbrodt, J.M. Pearce, Tensile strength of commercial polymer materials for fused filament fabrication 3D printing, *Additive Manufacturing*, 15 (2017) 40-47.
- [33] M. Domingo-Espin, J.M. Puigoriol-Forcada, A.-A. Garcia-Granada, J. Lluma, S. Borros, G. Reyes, Mechanical property characterization and simulation of fused deposition modeling Polycarbonate parts, *Materials & Design*, 83 (2015) 670-677.
- [34] A.N. Dickson, J.N. Barry, K.A. McDonnell, D.P. Dowling, Fabrication of Continuous Carbon, Glass and Kevlar fibre reinforced polymer composites using Additive Manufacturing, *Additive Manufacturing*, (2017).
- [35] C. Koch, L. Van Hulle, N. Rudolph, Investigation of Mechanical Anisotropy of the Fused Filament Fabrication Process via Customized Tool Path Generation, *Additive Manufacturing*, (2017).
- [36] M. Dawoud, I. Taha, S.J. Ebeid, Mechanical behaviour of ABS: An experimental study using FDM and injection moulding techniques, *Journal of Manufacturing Processes*, 21 (2016) 39-45.
- [37] A.R. Torrado, C.M. Shemelya, J.D. English, Y. Lin, R.B. Wicker, D.A. Roberson, Characterizing the effect of additives to ABS on the mechanical property anisotropy of specimens fabricated by material extrusion 3D printing, *Additive Manufacturing*, 6 (2015) 16-29.
- [38] B. Wittbrodt, J.M. Pearce, The effects of PLA color on material properties of 3-D printed components, *Additive Manufacturing*, 8 (2015) 110-116.
- [39] K.R. Hart, E.D. Wetzel, Fracture behavior of additively manufactured acrylonitrile butadiene styrene (ABS) materials, *Engineering Fracture Mechanics*, 177 (2017) 1-13.

- [40] T.D. McLouth, J.V. Severino, P.M. Adams, D.N. Patel, R.J. Zaldivar, The impact of print orientation and raster pattern on fracture toughness in additively manufactured ABS, *Additive Manufacturing*, 18 (2017) 103-109.
- [41] Y. Song, Y. Li, W. Song, K. Yee, K.-Y. Lee, V. Tagarielli, Measurements of the mechanical response of unidirectional 3D-printed PLA, *Materials & Design*, 123 (2017) 154-164.
- [42] A.K. Sood, R.K. Ohdar, S.S. Mahapatra, Parametric appraisal of mechanical property of fused deposition modelling processed parts, *Materials & Design*, 31 (2010) 287-295.

Figure captions

Figure 1. (a) hemp-PLA filament, (b) One of the forms and dimensions printed, (c) Mechanical testing showing the specimen prior and after tensile rupture.

Figure 2. Temperature measurement during the printing process: (a) Infra-red setup, and (b) related samples processed at different printing temperatures.

Figure 3. Thermal response of PLA-Hemp filament in DSC experiments.

Figure 4. Evolution of the PLA-Hemp temperature during the printing process for three different printing temperatures.

Figure 5. (a) Infra-red thermal signature from the laying down process of PLA-hemp filament for two extreme printing temperatures, (b) thermal cycling illustrated by the relative difference between the peak and ground temperatures for all printing temperatures.

Figure 6. (a) Tensile testing of a single PLA-hemp filament, and (b) comparison between the mechanical response of PLA and PLA-hemp filaments.

Figure 7. (a) Typical nodal results of the micromechanical model of the hemp-based filament, (b) Sensitivity analysis of the predicted Young's modulus as a function of the element size, (c) correlation between hemp-PLA interface properties and the predicted Young's modulus of the filament.

Figure 8. Optical micrographic images showing the change in morphology of the PLA-hemp composite induced by FDM at low (a) and (b) high printing temperatures.

Figure 9 Deformation sequences of 3D printed PLA-Hemp recorded using high speed camera (a) neat and (b) notched specimens.

Figure 10. Mechanical response of (a) neat and notched PLA-Hemp printed specimens as a function of the printing temperature.

Figure 11. Mechanical performance of printed PLA-Hemp with respect to data for polymers used in FDM (a) Young's modulus, (b) tensile strength, and (c) fracture toughness.

Figure 12. SEM micrographs of printed PLA-hemp at different magnifications.

Figure 13. (a) Cross-section views of the printed PLA-Hemp microstructure revealed using X-ray micro-tomography, (b) perspective view showing the void network within the printed structure.

Figure 14. (a) Schematics showing the geometrical variables used for the mathematical model representing the porosity network and justification from X-ray micro-tomography imaging, (b) 3D view of the mathematical model of microstructural arrangement, (c) Correlation between the porosity distribution and the printing temperature.

Figure 15. Axial porosity content profile in the main directions of a printed PLA-Hemp specimen at 230°C. Length, width and depth are expressed as a function of full dimensions (length= 18 mm, width = 13 mm, depth or thickness = 4 mm).

Figure 16. Effect of sample size on the stress component σ_{YY} distribution (voxel size is fixed to 14.31 μm , Y is the loading direction).

Figure 17. Normal stress component σ_{YY} for different resolutions (large voxel size represents a low resolution, Y is the loading direction).

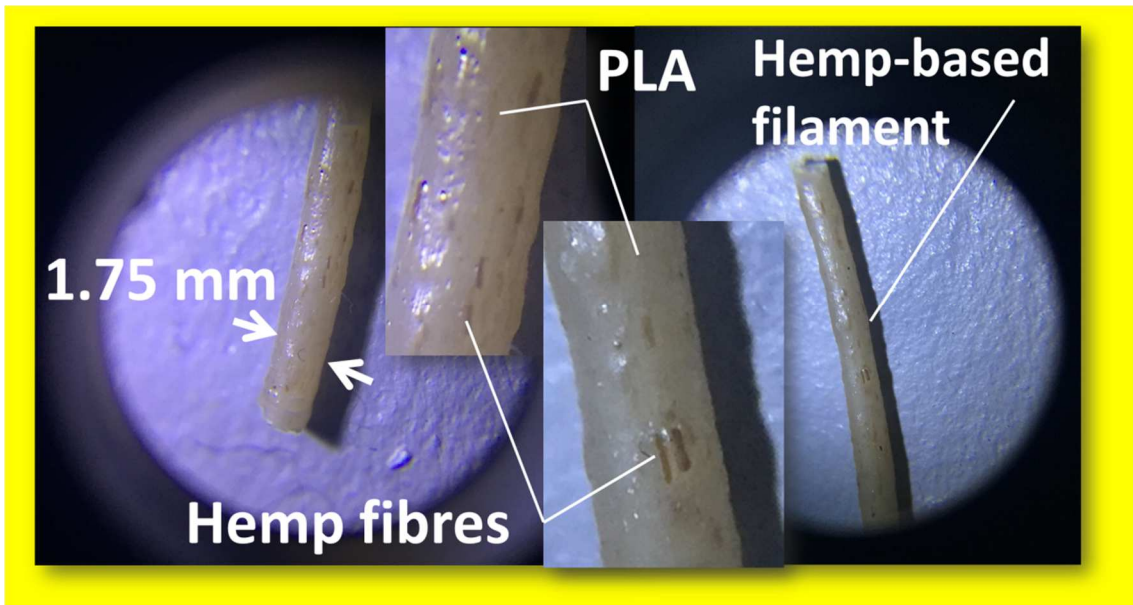
Figure 18. Error in Young's modulus as a function of (a) the voxel size and (b) specimen volume.

List of Tables

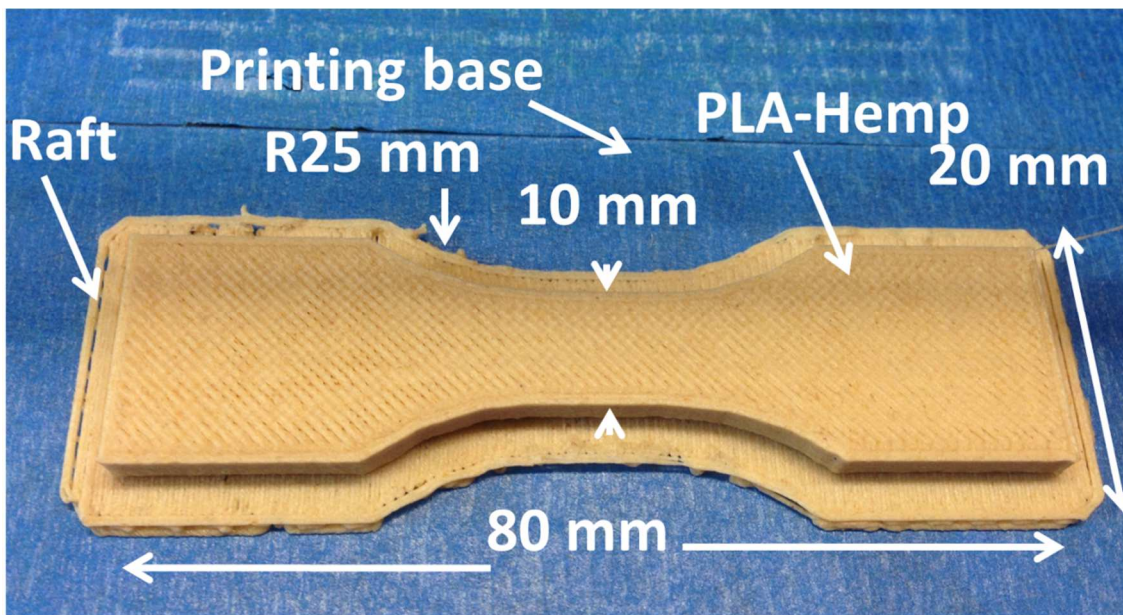
Table 1. Summary of measured properties of 3D printed PLA-Hemp material.

| Material | Printing temperature °C | Density (g/cm ³) | Porosity content* (%) | Young's modulus (MPa) | Tensile strength (MPa) | Elongation at break (%) | Fracture toughness MPa×m ^{1/2} |
|----------|-------------------------|------------------------------|-----------------------|-----------------------|------------------------|-------------------------|---|
| wire | - | 1.13 | 0 | 1000 ± 180 | 50 ± 3 | 6.42 ± 1.06 | - |
| printed | 210 | 1.06 ± 0.01 | 3.15 ± 0.04 | 795 ± 14 | 39 ± 1 | 5.10 ± 0.01 | 2.15±0.37 |
| | 220 | 1.10±0.04 | 6.09± 0.01 | 896 ±73 | 45 ±2 | 5.33 ± 0.10 | 2.56±0.06 |
| | 230 | 1.06±0.02 | 5.02± 0.02 | 883 ±12 | 45 ±3 | 5.34 ± 0.33 | 2.71±0.30 |
| | 240 | 1.03±0.02 | 8.73± 0.04 | 933 ± 30 | 48 ±2 | 5.65 ± 0.20 | 2.80±0.10 |

*based on density measurements.

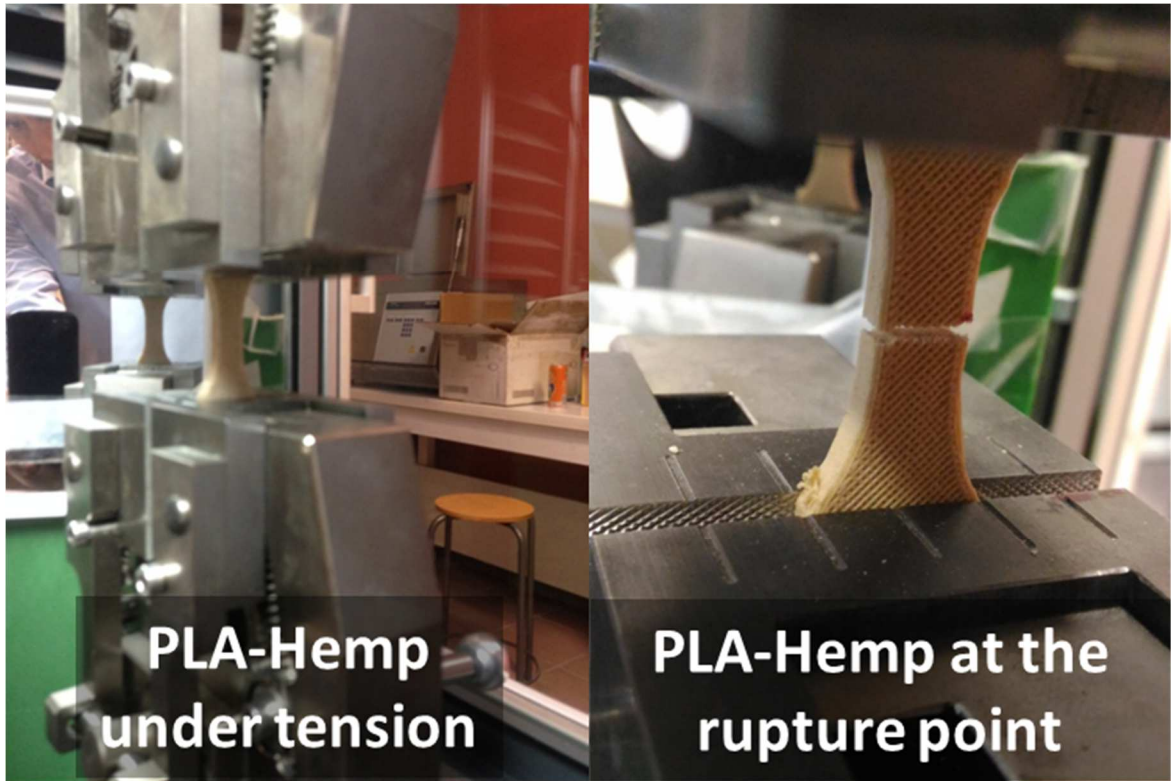


(a)



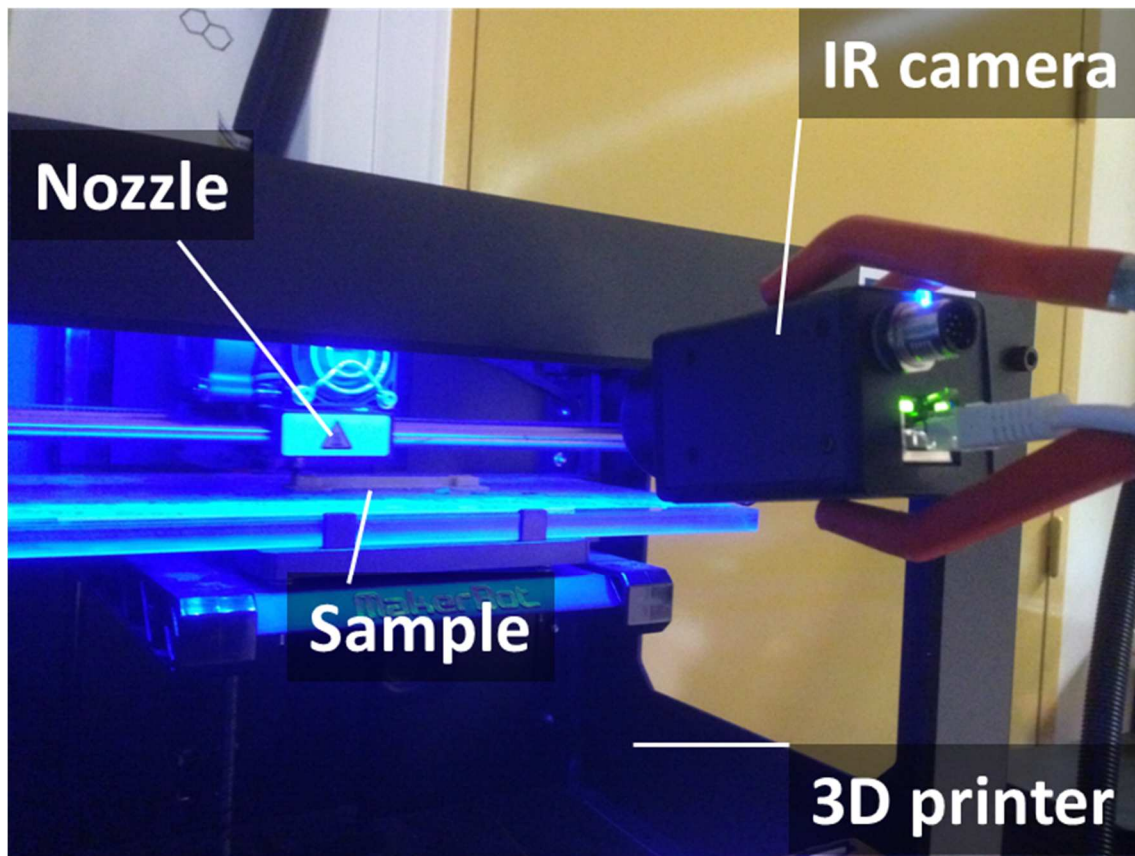
(b)

Figure 1. (a) hemp-PLA filament, (b) One of the forms and dimensions printed, (c) Mechanical testing showing the specimen prior and after tensile rupture.

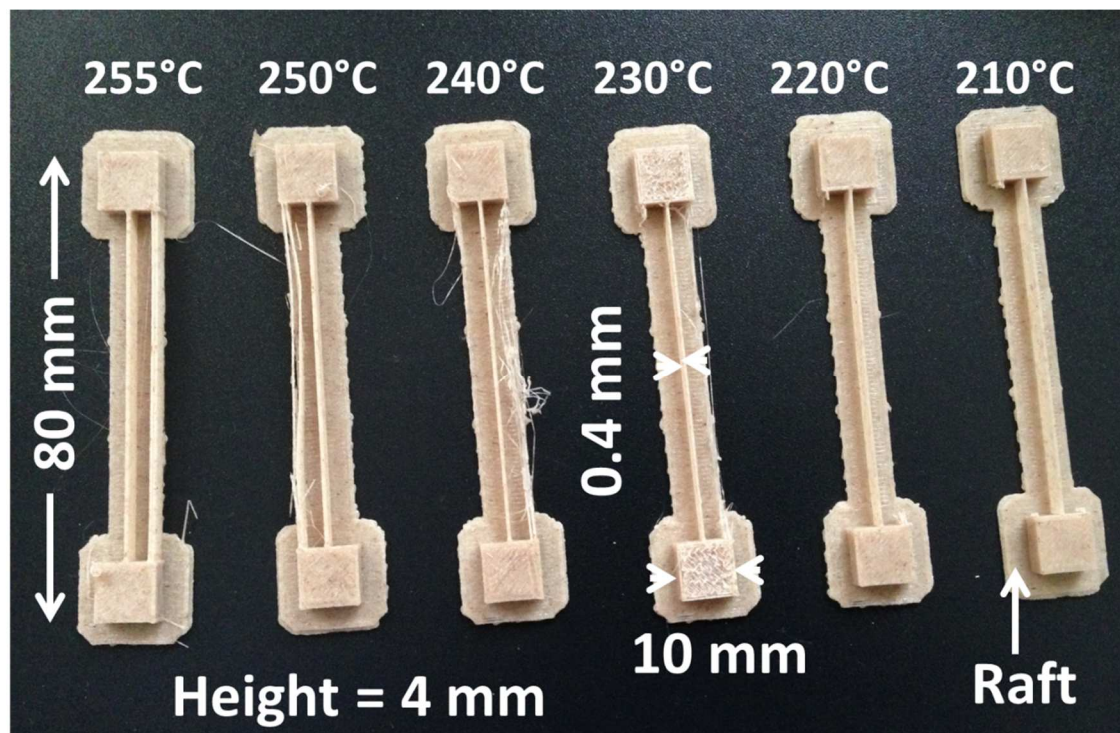


©

Figure 1. (continued).



(a)



(b)

Figure 2. Temperature measurement during the printing process: (a) Infra-red setup, and (b) related samples processed at different printing temperatures.

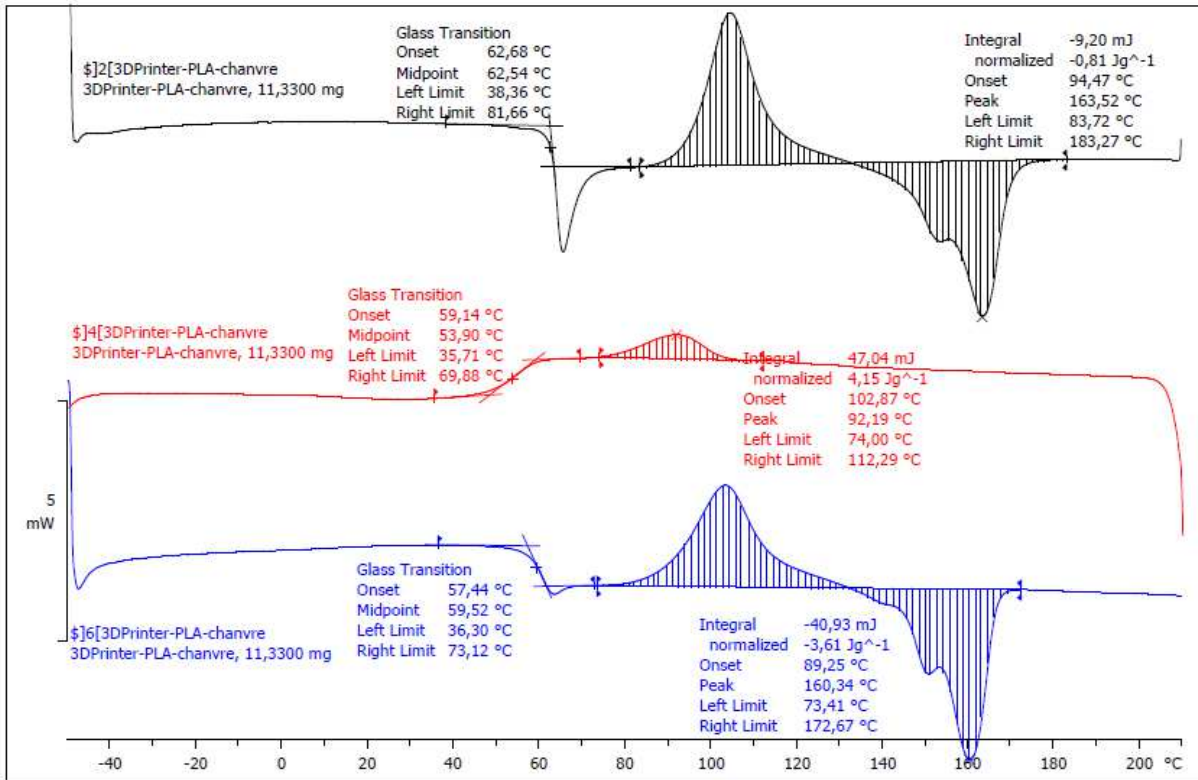


Figure 3. Thermal response of PLA-Hemp filament in DSC experiments.

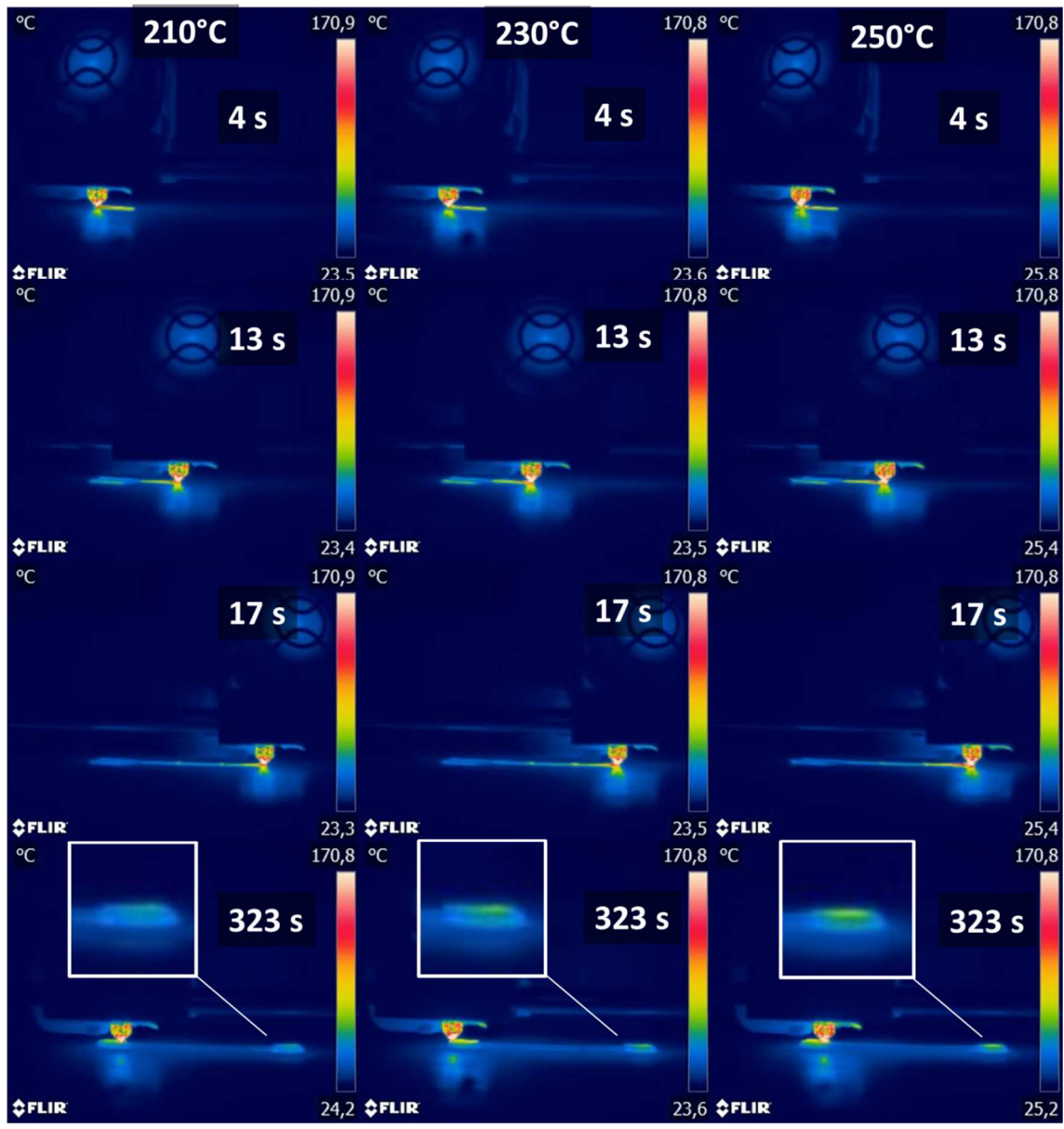
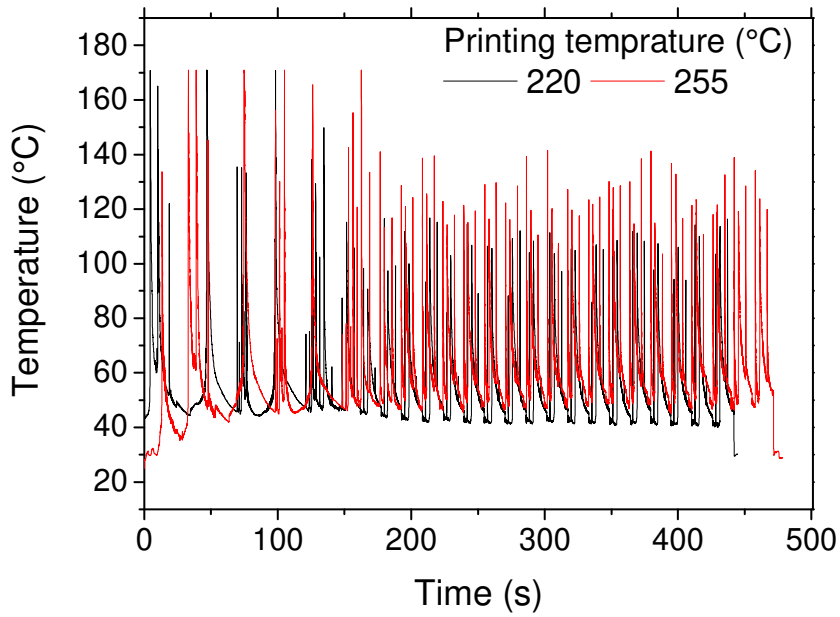
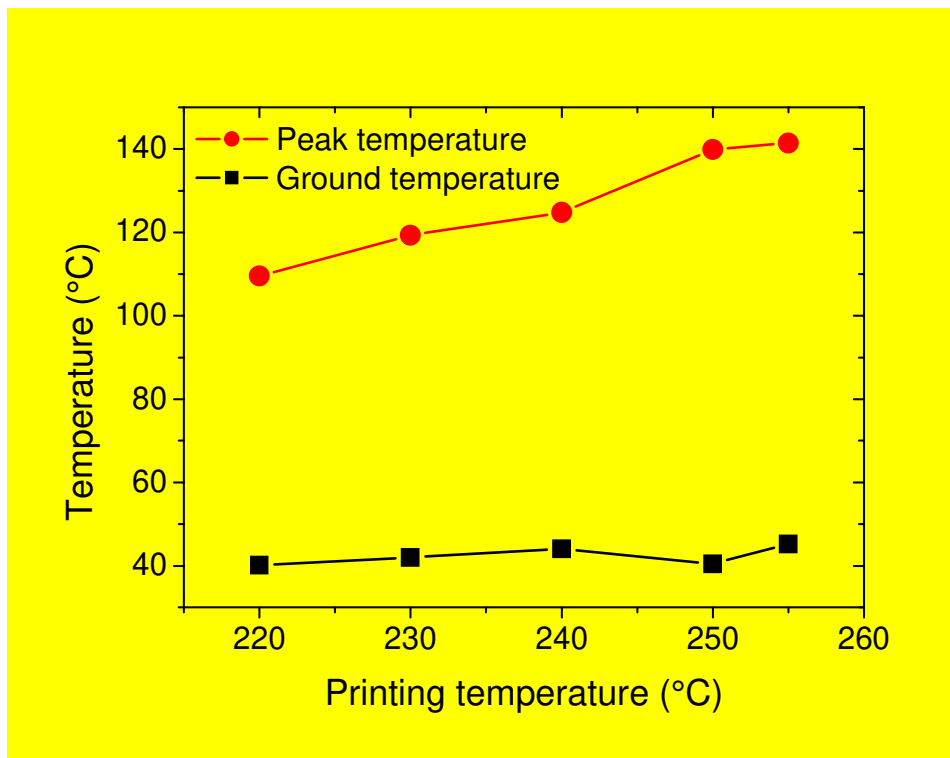


Figure 4. Evolution of the PLA-Hemp temperature during the printing process for three different printing temperatures.

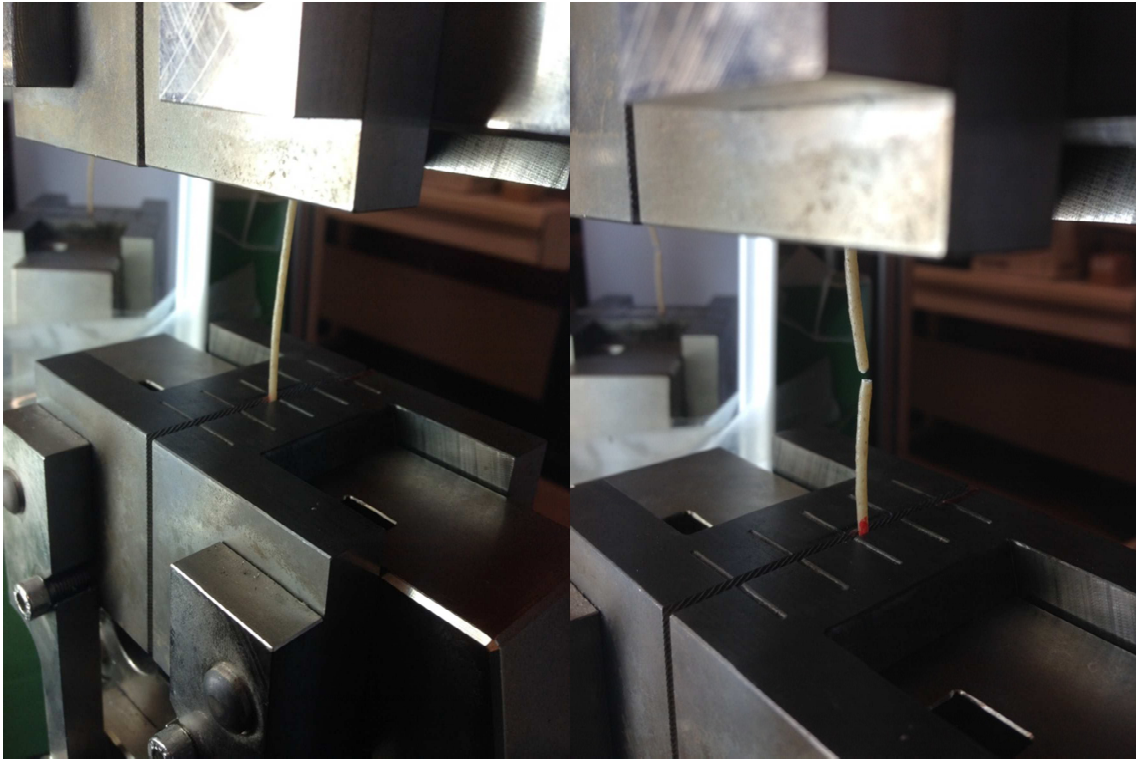


(a)

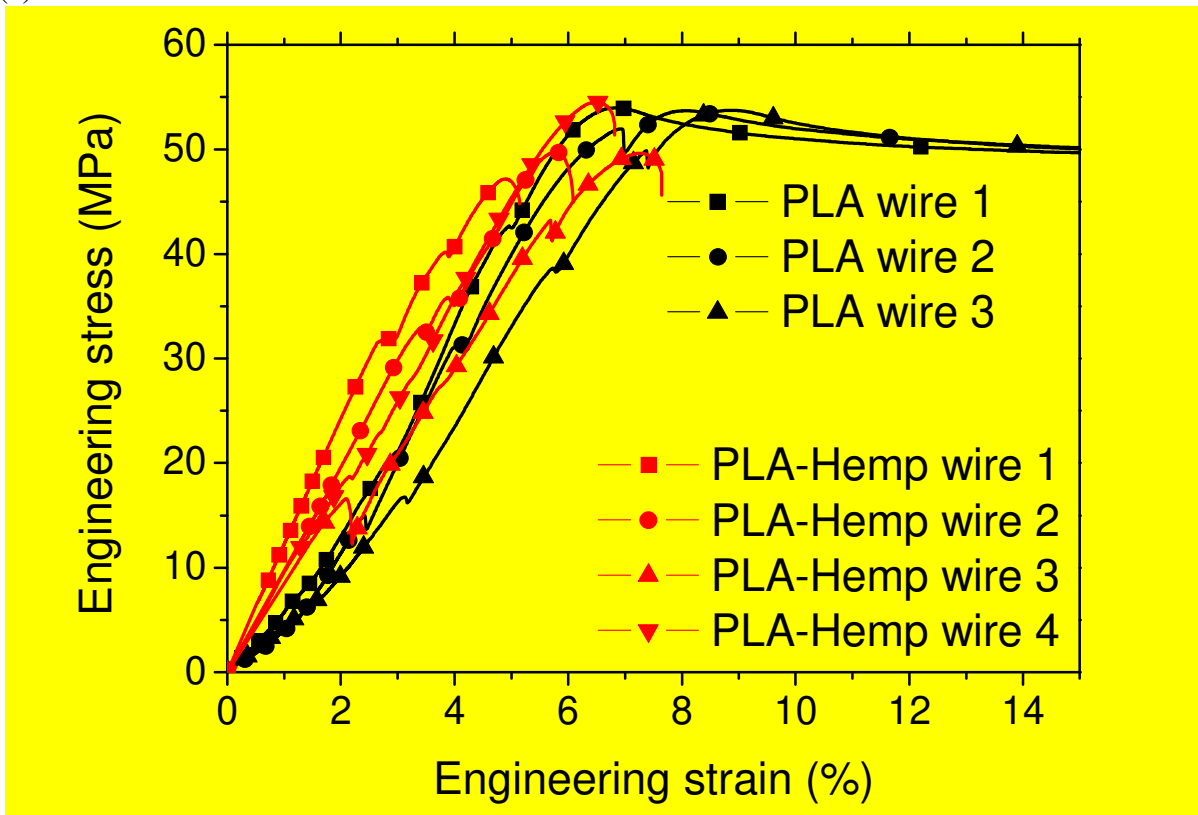


(b)

Figure 5. (a) Infra-red thermal signature from the laying down process of PLA-hemp filament for two extreme printing temperatures, (b) thermal cycling illustrated by the relative difference between the peak and ground temperatures for all printing temperatures.

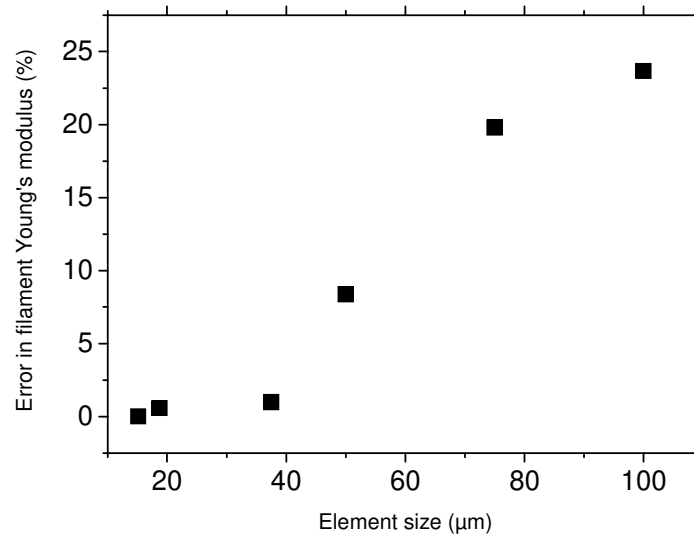
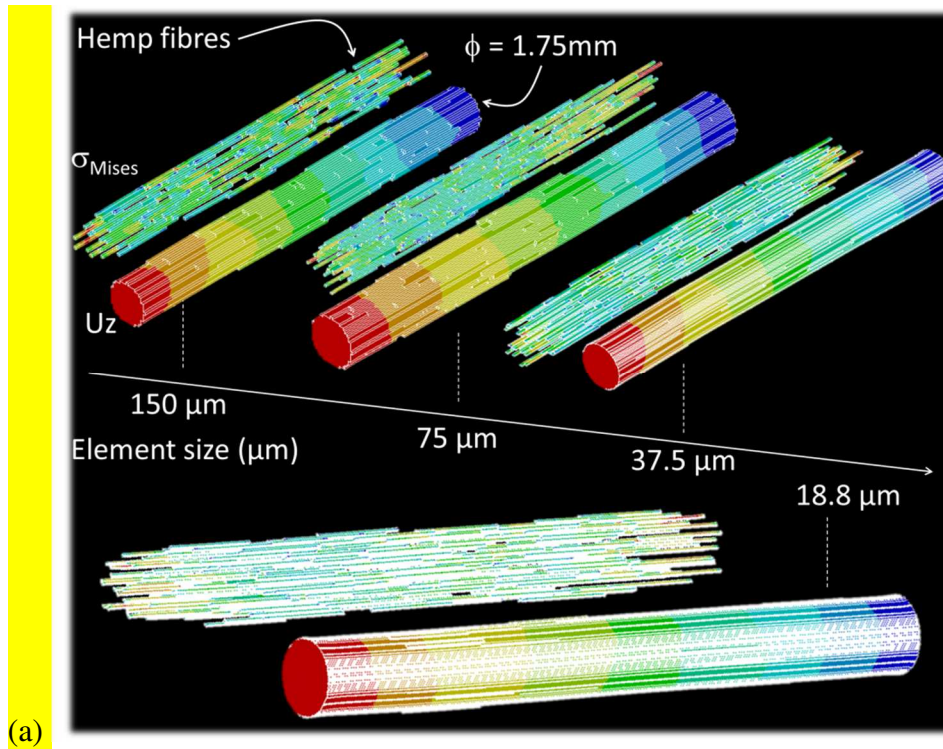


(a)



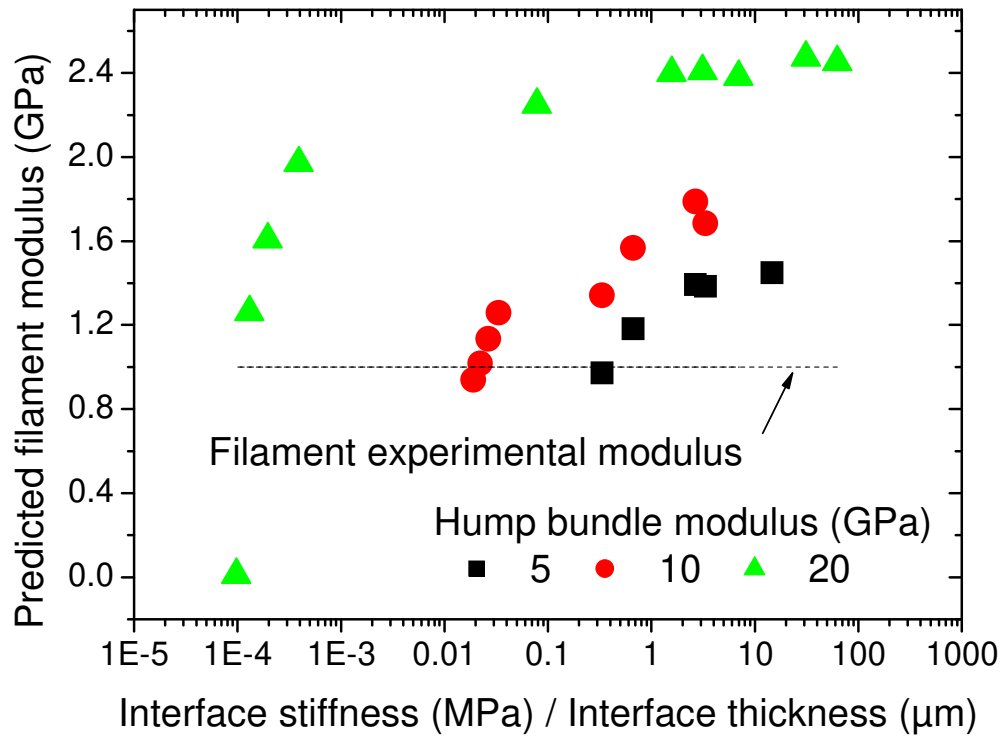
(b)

Figure 6. (a) Tensile testing of a single PLA-hemp filament, and (b) comparison between the mechanical response of PLA and PLA-hemp filaments.



(b)

Figure 7. (a) Typical nodal results of the micromechanical model of the hemp-based filament, (b) Sensitivity analysis of the predicted Young's modulus as a function of the element size, (c) correlation between hemp-PLA interface properties and the predicted Young's modulus of the filament.



(c)

Figure 7. (continued)

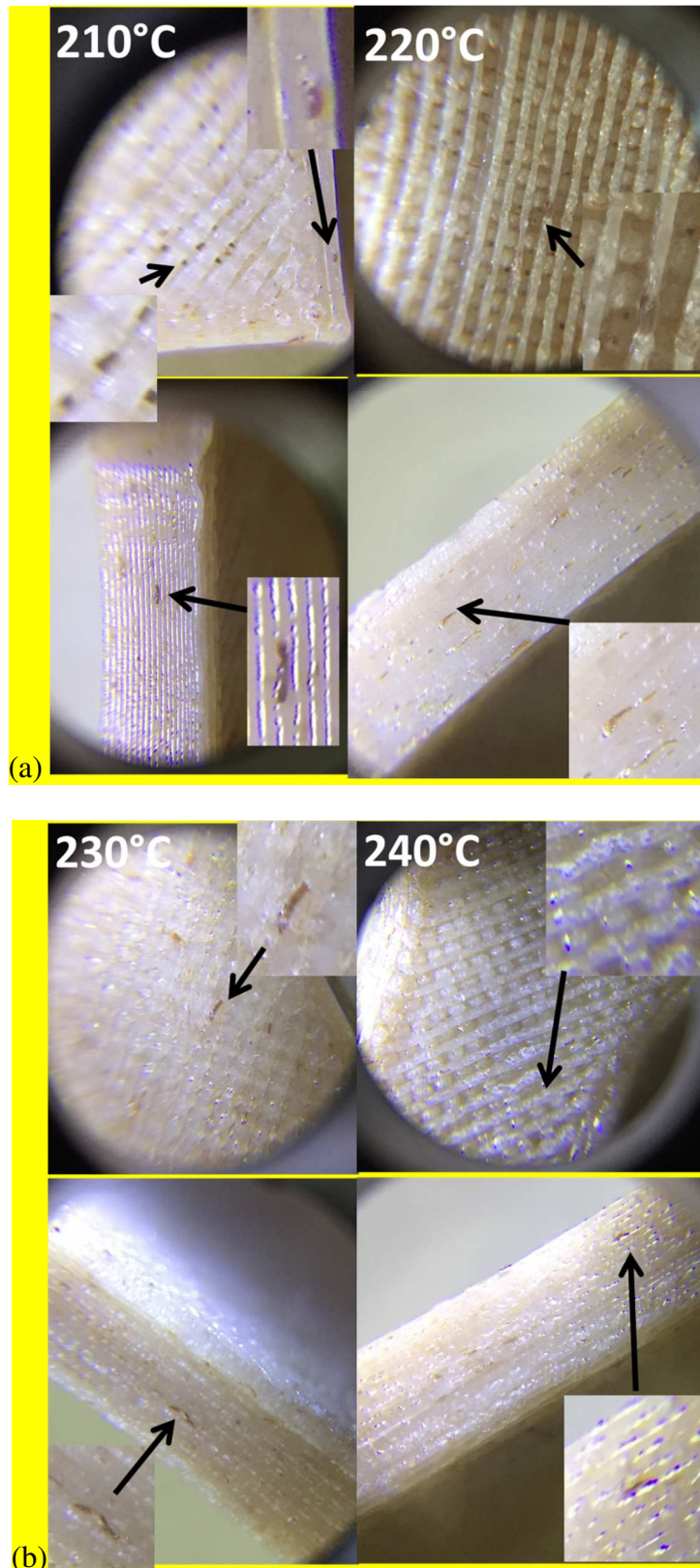
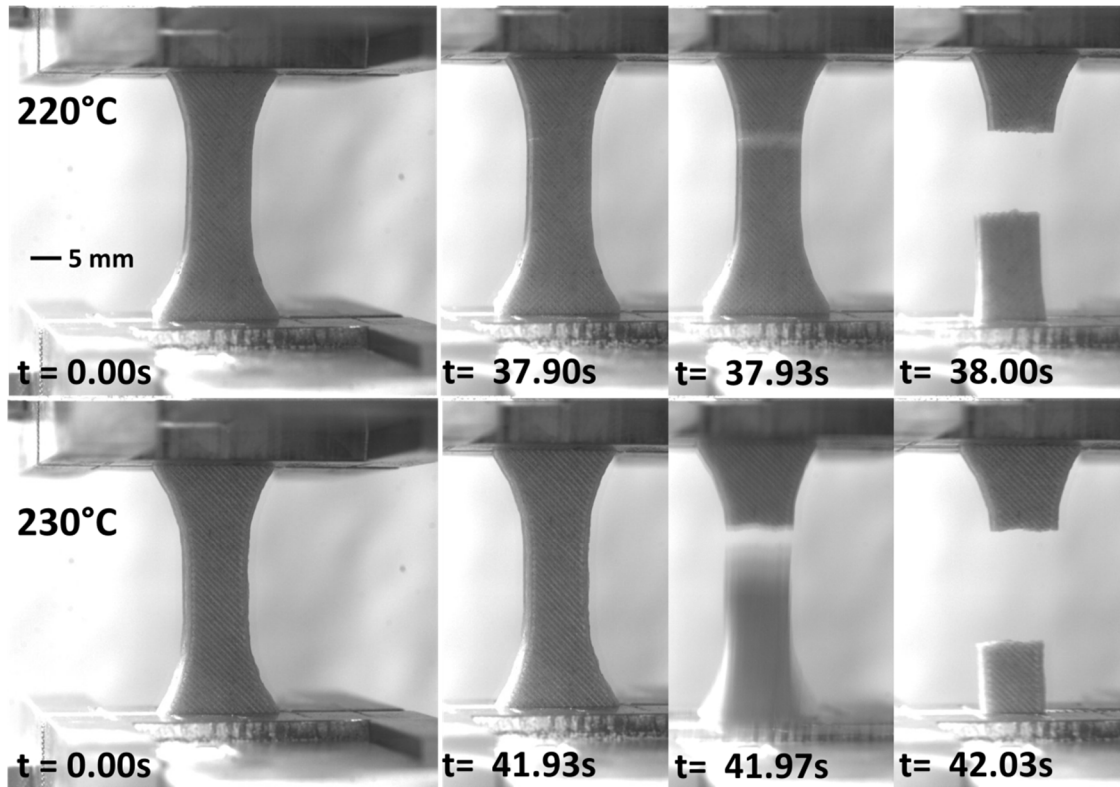
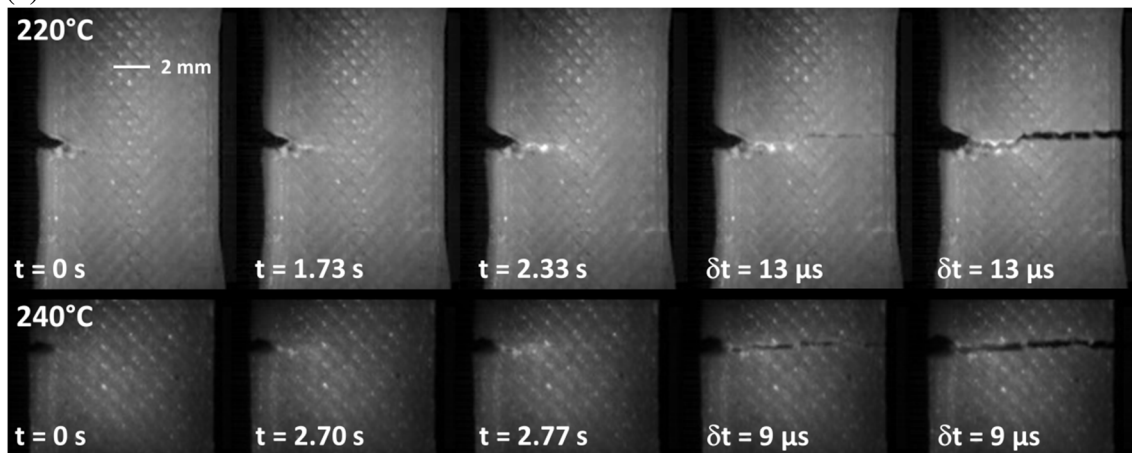


Figure 8. Optical micrographic images showing the change in morphology of the PLA-hemp composite induced by FDM at low (a) and (b) high printing temperatures.



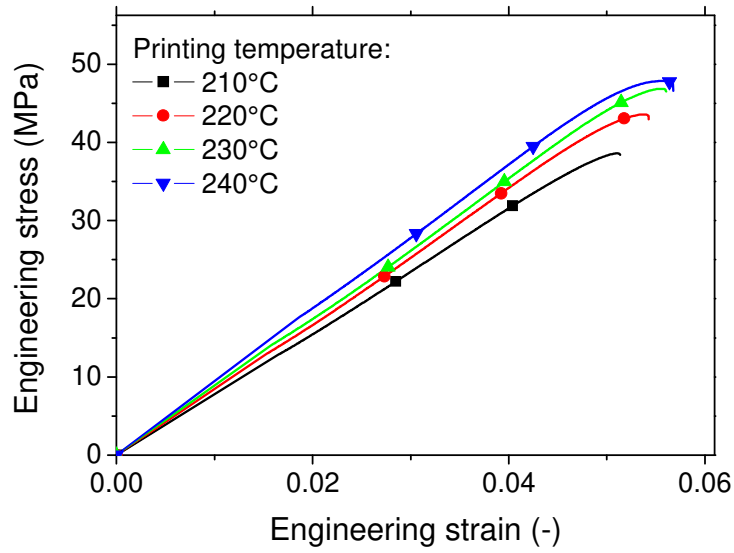
(a)



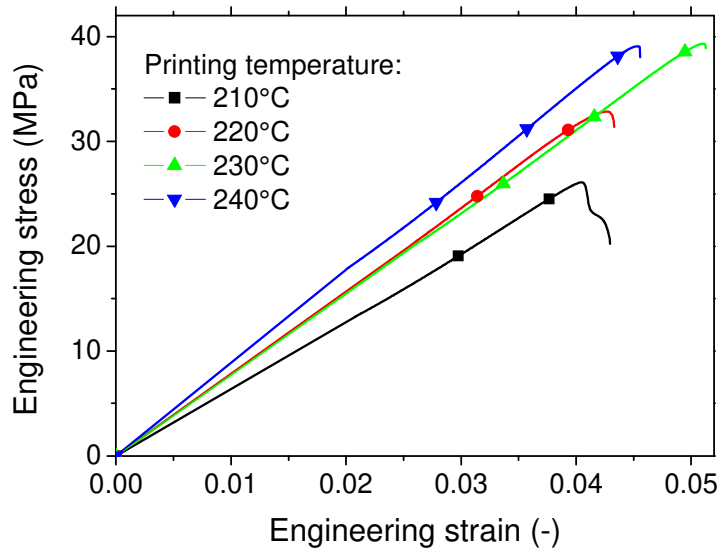
(b)

Figure 9 Deformation sequences of 3D printed PLA-Hemp recorded using high speed camera

(a) neat and (b) notched specimens.



(a)



(b)

Figure 10. Mechanical response of (a) neat and notched PLA-Hemp printed specimens as a function of the printing temperature.

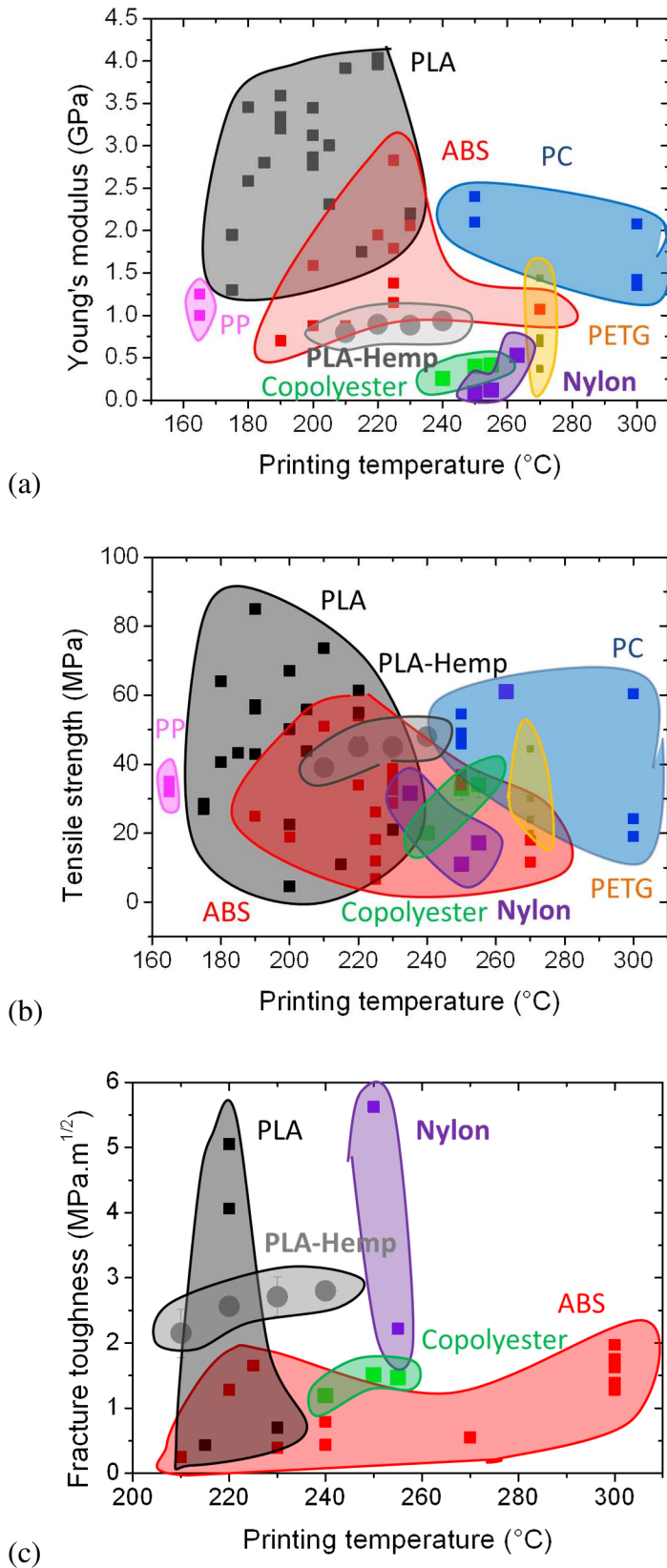


Figure 11. Mechanical performance of printed PLA-Hemp with respect to data for polymers used in FDM (a) Young's modulus, (b) tensile strength, and (c) fracture toughness.

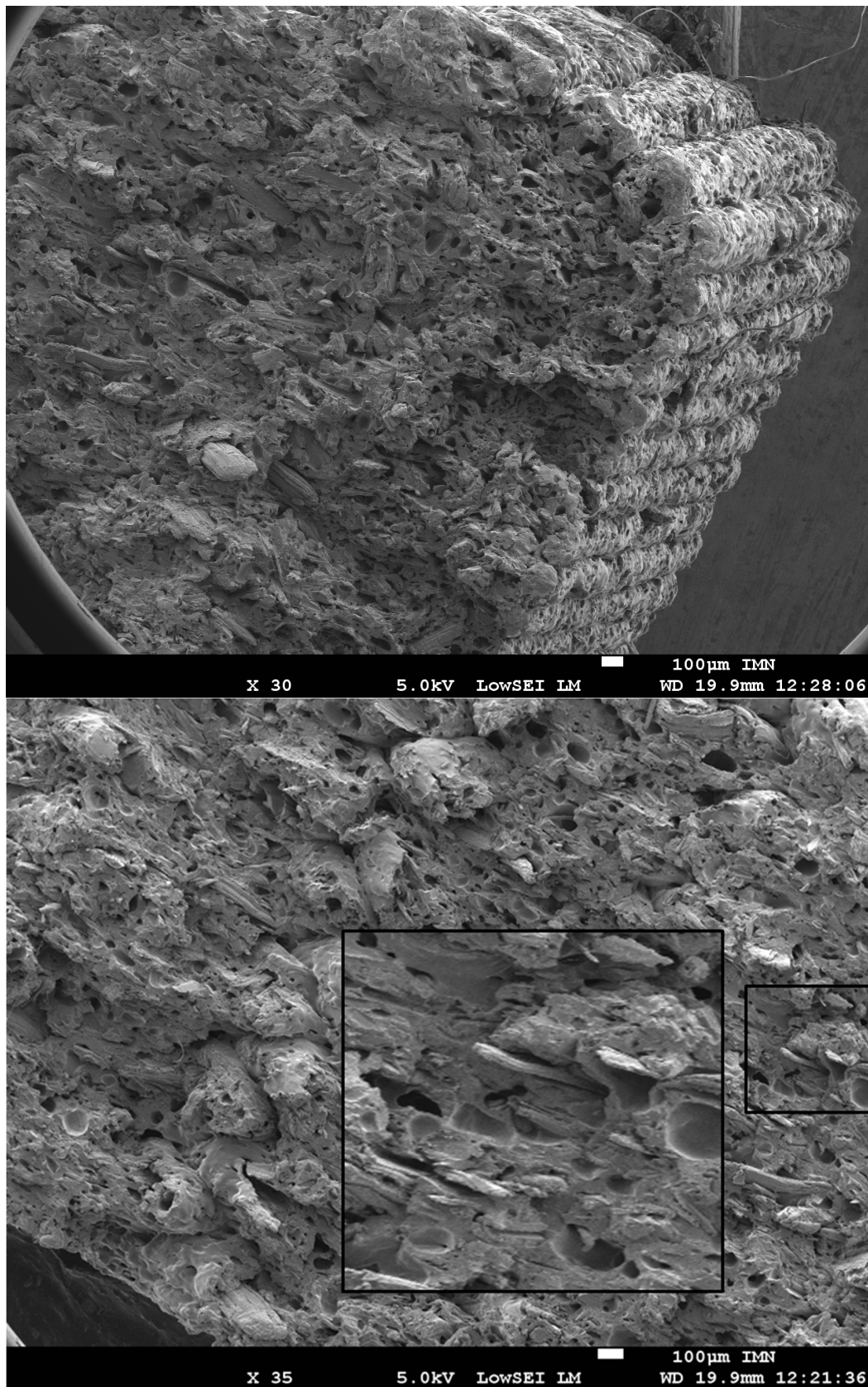


Figure 12. SEM micrographs of printed PLA-hemp at different magnifications.

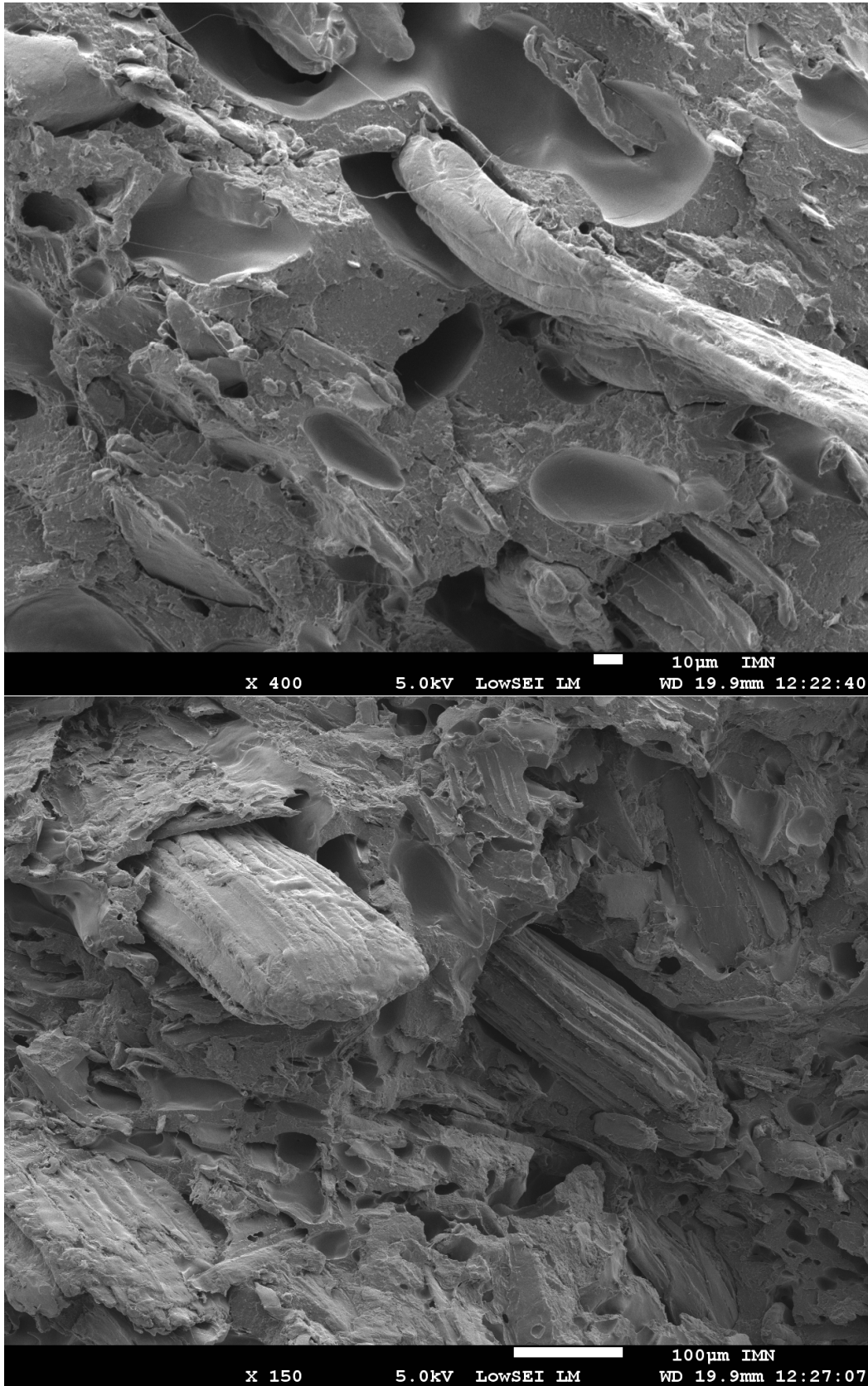


Figure 12. (continued).

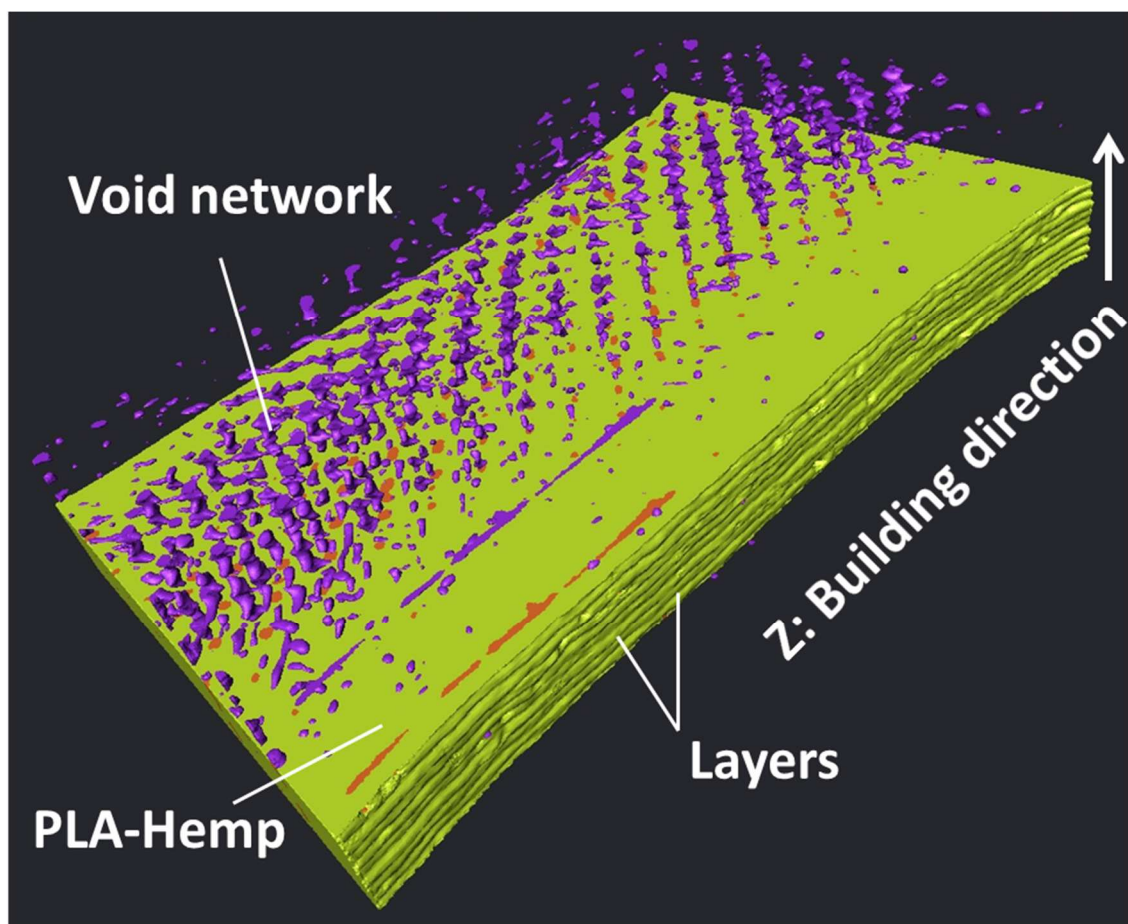
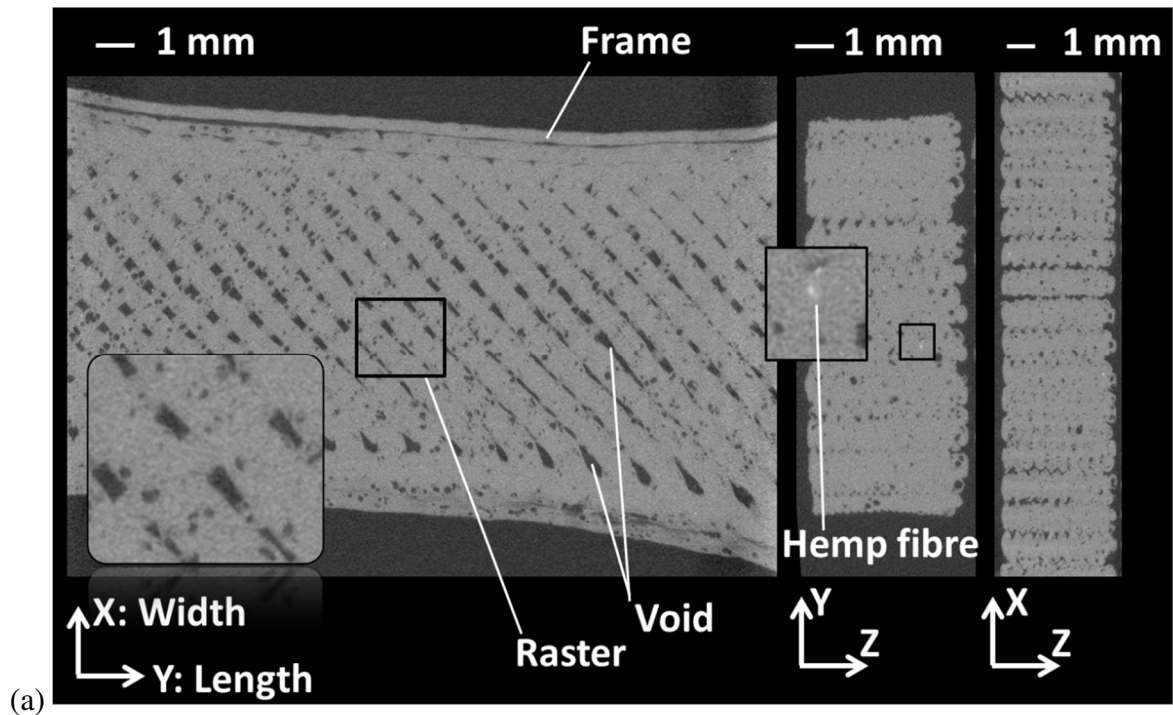
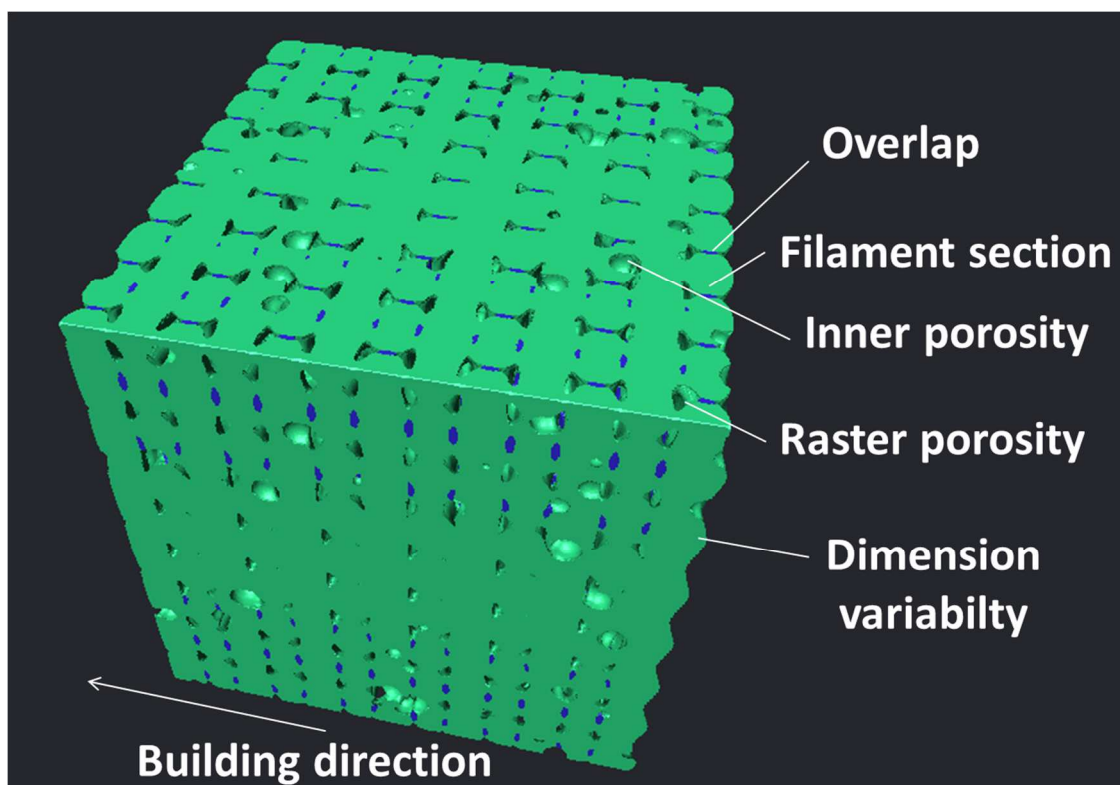
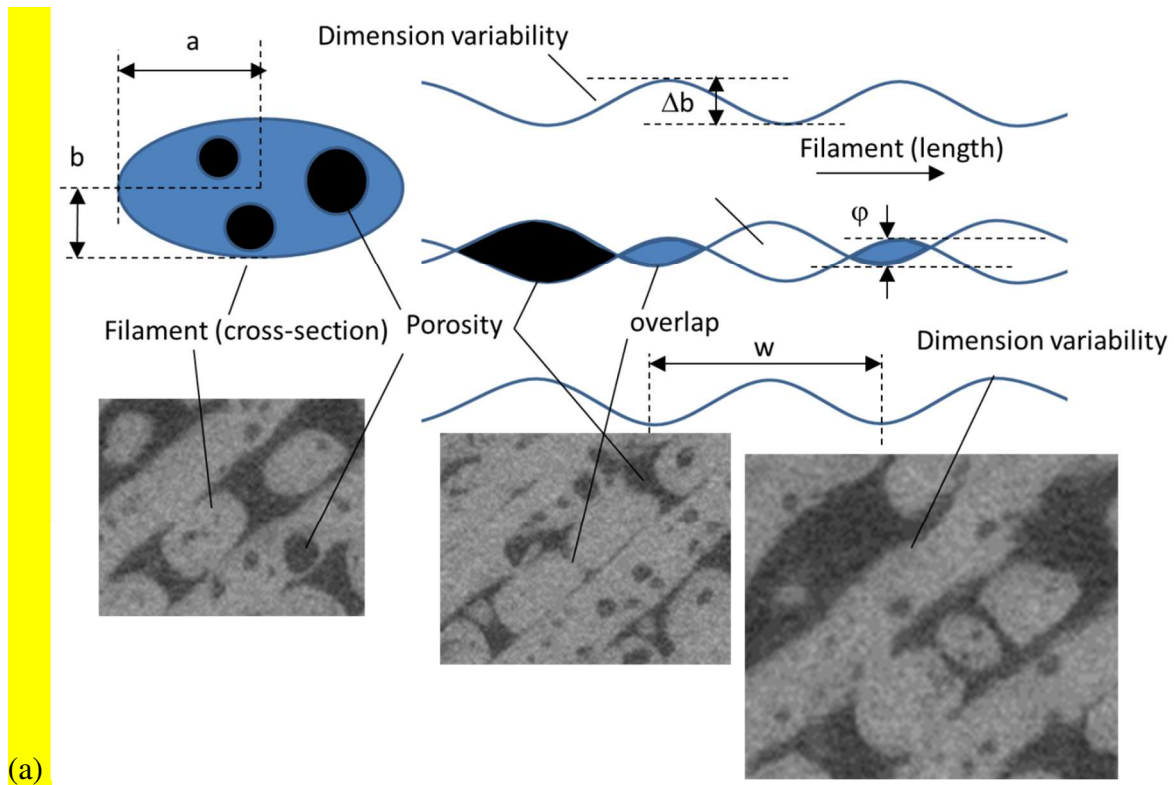
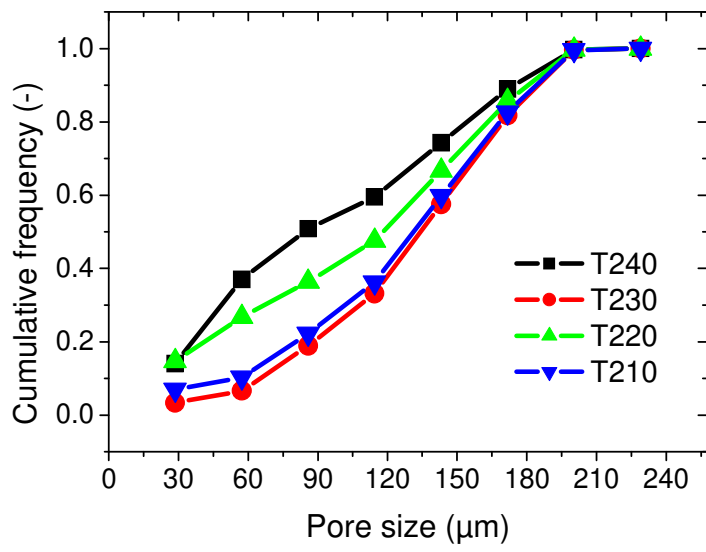


Figure 13. (a) Cross-section views of the printed PLA-Hemp microstructure revealed using X-ray micro-tomography, (b) perspective view showing the void network within the printed structure.



(b)

Figure 14. (a) Schematics showing the geometrical variables used for the mathematical model representing the porosity network and justification from X-ray micro-tomography imaging, (b) 3D view of the mathematical model of microstructural arrangement, (c) Correlation between the porosity distribution and the printing temperature.



(c)

Figure 14. (continued)

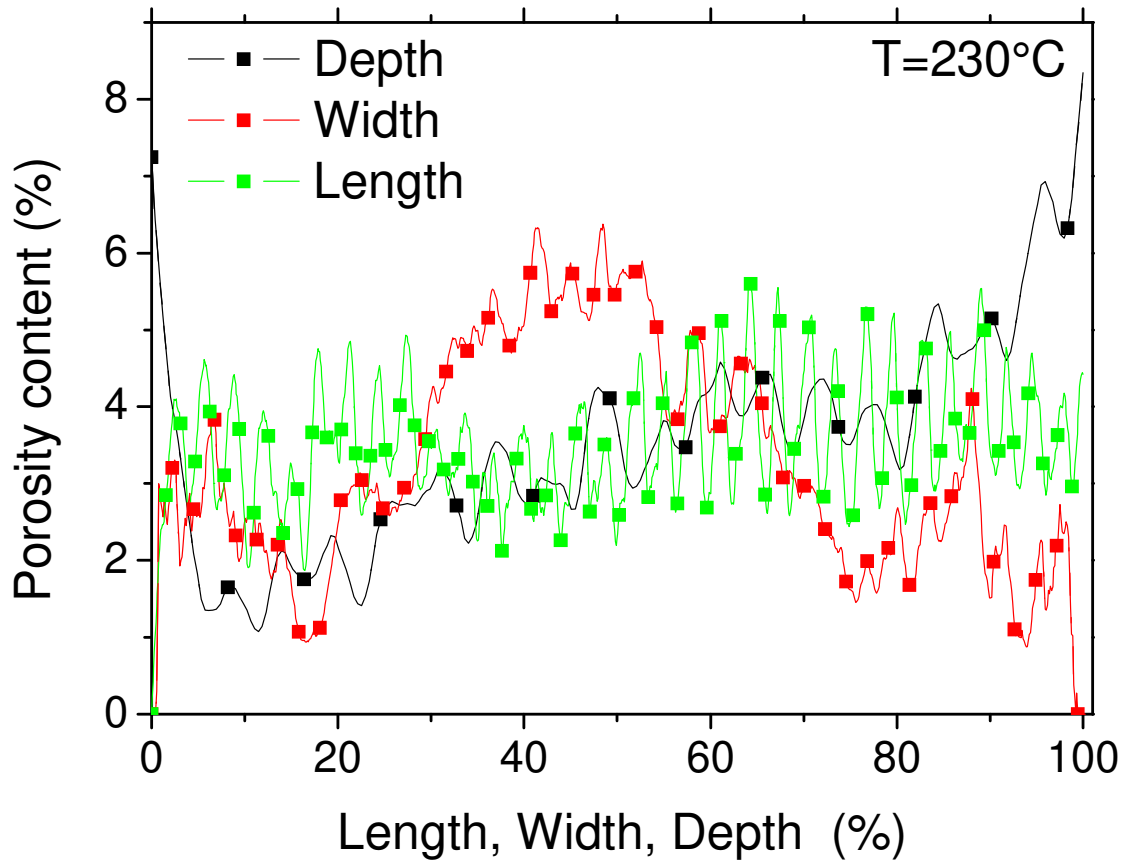


Figure 15. Axial porosity content profile in the main directions of a printed PLA-Hemp specimen at 230°C. Length, width and depth are expressed as a function of full dimensions (length= 18 mm, width = 13 mm, depth or thickness = 4 mm).

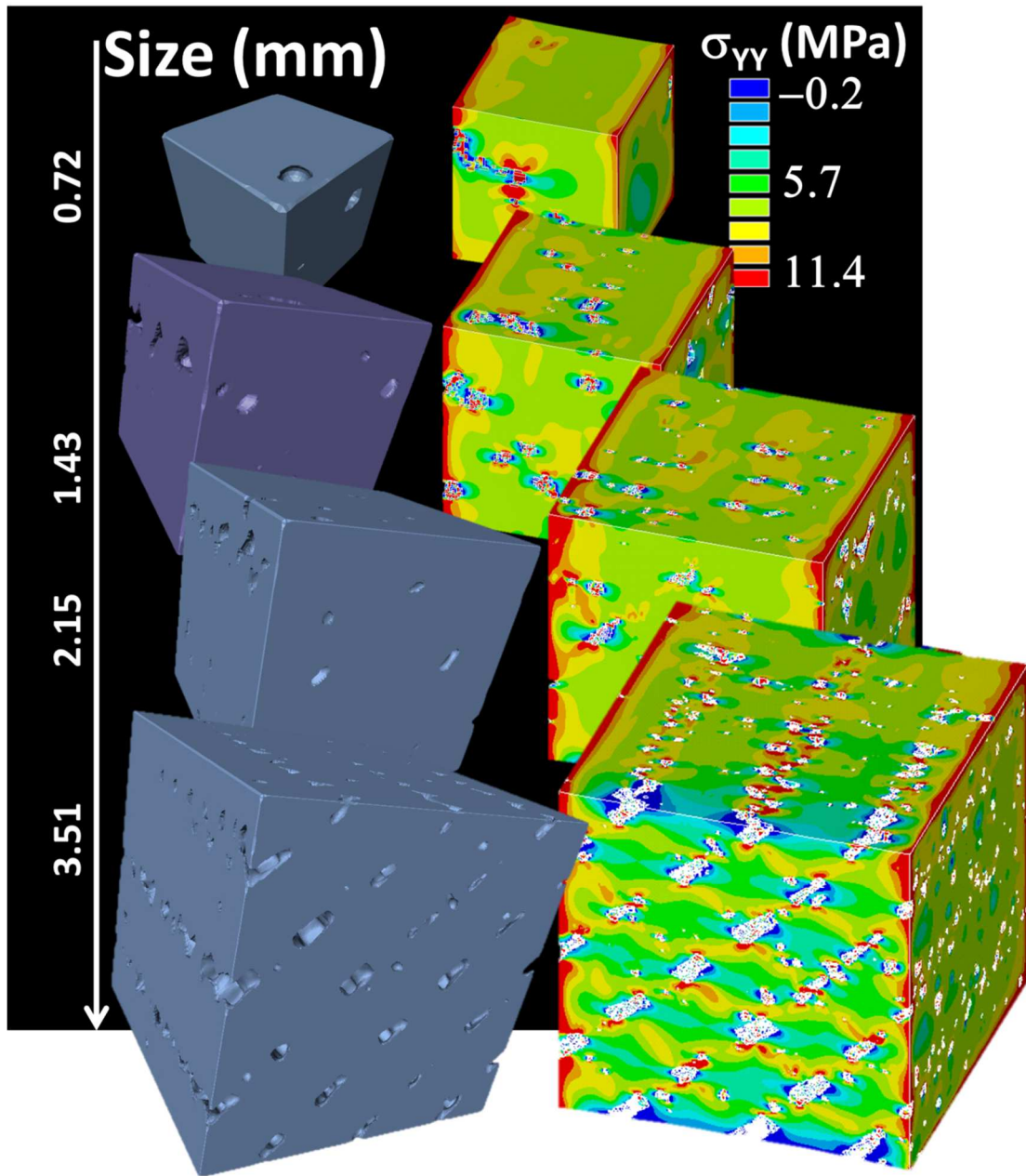


Figure 16. Effect of sample size on the stress component σ_{yy} distribution (voxel size is fixed to 14.31 μm , Y is the loading direction).

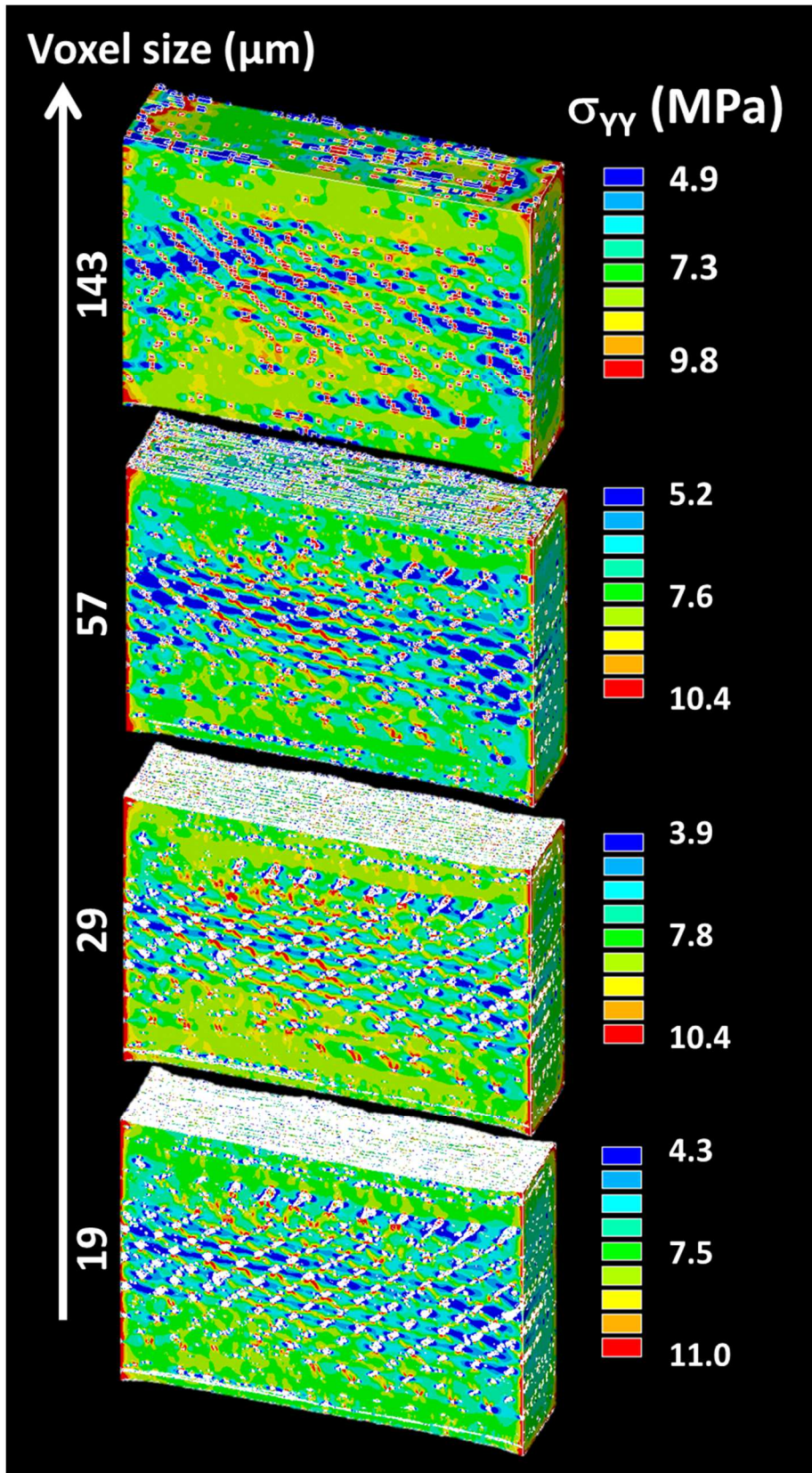
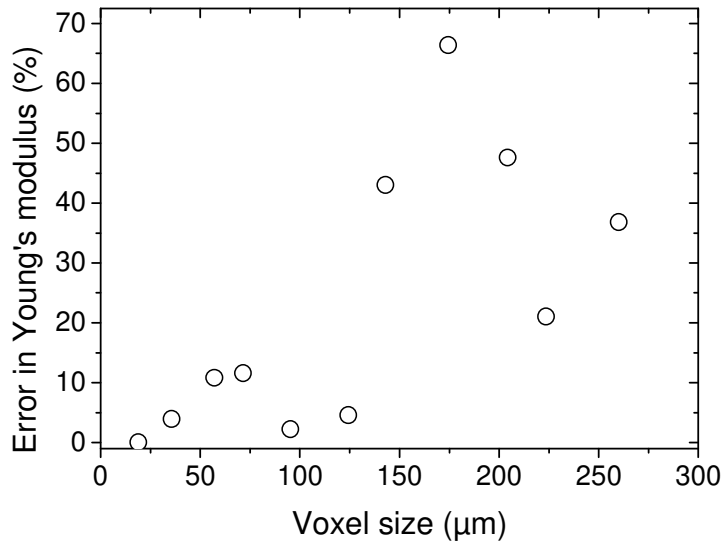
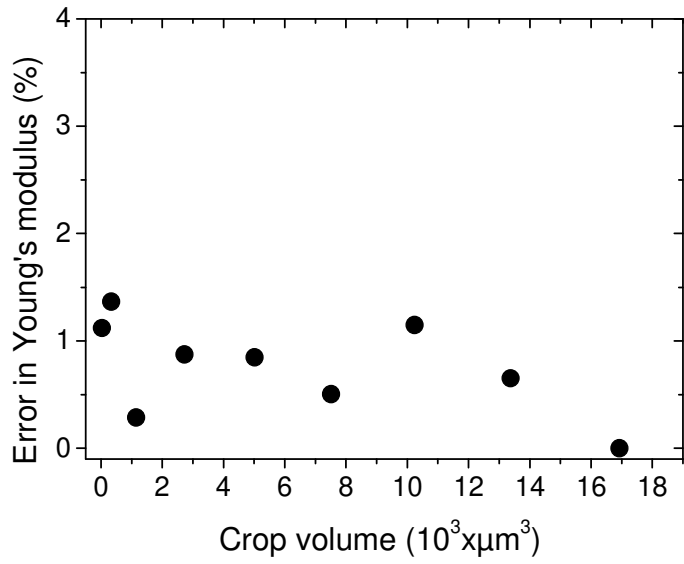


Figure 17. Normal stress component σ_{YY} for different resolutions (large voxel size represents a low resolution, Y is the loading direction).



(a)



(b)

Figure 18. Error in Young's modulus as a function of (a) the voxel size and (b) specimen volume.